J Intell Robot Syst (2017) 88:73–95
DOI 10.1007/s10846-017-0546-1

Dynamics and Control of a 6-dof Cable-driven Parallel Robot with Visco-elastic Cables in Presence of Measurement Noise

M. Habibnejad Korayem · M. Yousefzadeh · B. Beyranvand

Received: 4 July 2016 / Accepted: 21 March 2017 / Published online: 25 April 2017

Abstract Cable robots are a type of parallel robots where the rigid links are replaced by flexible cables. This flexibility produces internal dynamic which challenges the rigid model based controller. In this paper, the dynamic equations of cable robots with viscoelastic cables are obtained. The Feedback Linearization (FL) method is used to provide a linearized dynamic error for the closed loop model of the system with rigid cables. Using the Lyapunov criterion, the stability analysis of the flexible system with the rigid FL control input is performed. It is shown that considering a minimum damping coefficient and employing the rigid FL controller, the system stability can be guaranteed. In order to achieve a trade-off between the control input and the tracking error, the FL gains are obtained using LQR method. In practice, measurement noise usually exists. On the other hand, the end-effector vibration caused by the cables elasticity can be considered as a process noise. Therefore, the LQG approach is used to estimate the states in presence of the process and measurement noise. Using simulation, it is shown that in presence of measurement noise, the LQG method effectively controls the system while the LQR and also the SMC approach, employed in Korayem et al. (Robotica **33**(3), 578–598, 2015), lead to the system instability. Another simulation demonstrates that the system with damping less than the specified minimum value can be stable with the LQG approach, in contrary to the LQR controller. Moreover, in order to investigate the vibrational effect of the cable stiffness and damping coefficient, a frequency analysis is performed. Finally, experimental result obtained by implementation on a manufactured cable robot is presented and verified the approach.

Keywords Cable-driven parallel robot · Feedback Linearization · LQR · Kalman filter · LQG

M. H. Korayem (✉) · M. Yousefzadeh · B. Beyranvand
Robotic Research Laboratory, Center of Excellence in Experimental Solid Mechanics and Dynamics, School of Mechanical Engineering, Iran University of Science and Technology, Tehran, Iran
e-mail: hkorayem@iust.ac.ir

M. Yousefzadeh
e-mail: myousefzadeh@iust.ac.ir

1 Introduction

Cable robots benefit from features such as low weight, easy assembling, low production cost, and sufficient accuracy in many applications like in cranes, studio cams, medical equipment, etc. However, there is a fundamental difference in the actuator mechanism of these types of parallel robots and serial link robots, i.e. in contrast to the serial link robots, the cable robots can only tolerate tensile forces. In addition, cable flexibility may result in the cable tension oscillation and end-effector vibration. This can be more destructive in the under-constrained types, where the tension of the cables cannot be increased using the system redundancy.

The cable flexibility increases the number of the state variables. Thus far, control of flexible CDPRs required auxiliary feedback in addition to the actuator feedback, such as cable tension or the direct measurement of the end-effector pose. Therefore, in addition to more required sensors, the control input complication also enhances the processor computations. On the other hand, in the case of rigid model based controller, the system flexibility adds internal dynamic to the closed loop system. Therefore, it should be shown that the created internal dynamic is stable and also it would not lead to instability of the system output. This paper proposes a condition under which the flexible CDPRs stay stable by solely a rigid model based controller even in the presence of measurement noise. Subsequently, it needs less feedback sensors to guarantee the system stability, compared with the previous studies.

The cable flexibility has been incorporated into the dynamic model differently. Diao studied the vibration of cable-driven robots, caused by cables flexibility, and showed that the cables lateral vibration compared with the axial vibration can be ignored [1]. Zhang modeled the cables flexibility separately and then combined the flexible cable model and the rigid dynamic equations [2]. Miermeister et al. proposed to obtain the cable force as a combination of nonlinear spring and hysteresis force [3]. The hysteresis function was considered to be dependent on the excitation amplitude and frequency. In applications with very large workspace, the cable mass beside the flexibility should be taken into account. In [4], stiffness and workspace analysis of a 3-dof spatial cable robot was performed considering sagging effect caused by the cable mass. In [5], Huang et al. modeled the cable in the tethered space robots by a number of mass points connected via massless linear springs.

In order to maintain the stability of the flexible system, the researchers have incorporated the added degrees of freedom in the flexible model based controller. Korayem et al. obtained the dynamic equations of a 6-dof cable-suspended robot with elastic joints, and controlled the end-effector using a robust Feedback Linearization method [6]. They also modeled the cables vibration with partial differential equations (PDE) and used the tension obtained from PDE solution in the Sliding Mode controller (SMC) in order to compensate for the flexibility uncertainties [7]. The control laws proposed by the authors in [6, 7], need the feedback obtained from motor rotations together with the direct feedback of the end-effector pose. In these control laws, the end-effector acceleration is also required. This data can be supplied in two ways: 1) By second derivative operation on the end-effector pose [6]. In the implementation, this operation on the data with the inevitable measurement noise can cause significant error in the control input calculations. Therefore, the noise filtration should have been applied. 2) By means of Load Cell sensors for measuring the cable forces imposed on the end-effector, the end-effector pose and the end-effector dynamic equation [7]. In summary, the approach in [6] needs two measurement data, i.e. motor rotations and the end-effector precise pose, whereas the approach in [7] needs the two measurement data together with the Load Cell measurements.

Control of flexible cable robots can also be accomplished using the measurements of the cables tension. Laroche et al. modeled the cables as springs and controlled the robot by H_∞ method, using the feedback from the end-effector pose and the mean tension of the cables for a 3-dof cable robot with a point mass end-effector [8]. Meunier et al. derived the equations of the reflector of a large radio telescope by discretizing the cables using lumped mass elements, where springs and dampers are placed between them [9]. They employed a cascade approach, including cable tension control using H_∞ method in the inner loop, and end-effector pose control using inverse dynamic plus a PID in the outer loop. Lumped-mass method was also employed by Caverly et al. in modeling the cables of a 2DOF planar cable-driven robot [10]. In this work passivity-based control method was applied using the feedback from motor rotations as well as the end-effector pose. In order to stabilize the internal dynamic of cable robots with elastic cables, Khosravi employed an auxiliary controller with the rate of the feedback obtained from the cables tension [11]. In [8] and [9] the additional feedback of the cable tension was employed, whereas in [11] the time derivative of cable tension has been used to guarantee the system stability.

Due to the presence of measurement noise and high frequency vibration in many robotic applications, the feedback data and closed loop stability may encounter difficulties. Therefore, the researchers address these issues by a proper state estimation method or robustifying the controller. State and parameter estimation of

a cable-driven mechanism was performed by Kosari et al. using Unscented Kalman filter and model predictive control [12]. This approach was also employed for a cable based transmission system in a surgical robot [13]. Tracking control of the constrained cable robots in presence of noise and system uncertainties was also addressed by Schenk using a robust adaptive sliding mode control [14]. Control of linear systems in presence of measurement and process noise can be accomplished using LQG method. This controller consists of LQR controller and Kalman state estimator. In this regard, Ternero proposed a non-standard LQG approach for path tracking of mobile robots [15]. Lambert compared PID and optimal LQG controllers for positioning task of a three-cabled balloon with elastic cables, and showed an improvement of 50% with LQG method [16]. In [17], Berg et al. presented the LQG based motion planning, where a-priori probability distributions of the state of the robot along the desired path is used for computing the probability of collisions. Their case studies included wheeled mobile robots and a 6-dof articulated robot. For control of cable transporter systems with longitudinal flexibility, Pota et al. proposed combined LQG/H_∞ approach, where the H_∞ controller overcomes the system uncertainty and LQG controller improves performance of the system [18].

The existence of measurement noise can have destructive impact on the closed-loop response of the flexible systems, particularly during the derivative operations. In the control input calculations, the required end-effector acceleration in [6, 7] and the cable tension rate in [11], require derivative operation. The contribution of this paper in comparison to the previous researches as well as the authors' works in [6] and [7] are addressing the measurement noise problem using Kalman filter and decreasing the required feedback sensors. The Lyapunov stability analysis ensures that considering a minimum cable damping the system stability is achieved using only the feedback for the rigid model based controller. This feedback data is obtained from motor encoders and the direct kinematic equation. Moreover, the stability condition of the flexible system can be more relaxed using the Kalman filter. This is shown in a simulation by violation of the minimum damping condition.

The rest of this paper is organized as follows: In Section 2, dynamics of under-constrained 6-dof cable robots with viscoelastic cables is obtained. The stability analysis using Lyapunov criterion is presented in Section 3. In Section 4, the LQG approach is employed to address the measurement noise as well as the process noise caused by vibrations. Comparative simulations are provided in Section 5 to verify the advantages of LQG method over LQR controller as well as the SMC method employed in [7]. Also, the effect of the end-effector position on the system frequency and damping ratio is demonstrated using a frequency analysis in Section 5. Finally, verification of the approach by experiment is presented in Section 6.

2 Kinematic and Dynamic Equations

In this paper, the under-constrained type of the cable robots is investigated. However, the results can be considered for the fully-constrained types, employing the kinematic redundancy, to obtain optimal positive tension. The schematic view in Fig. 1 shows the general location of the cable endpoints for an under-constrained cable robot. Although these locations can be chosen arbitrarily, it has been observed that when the geometrical shape changes from regular hexagonal to triangular configuration, the workspace volume increases. In this study, the triangular configuration is considered in the simulation and experiment. The triangular end-effector is moved by six flexible cables. Each cable is modeled with a spring-damper element where the elasticity and damping coefficient have inverse relation with cable length. The center of the coordinate system attached to the end-effector is denoted by O_B, where the Center of Gravity (C.G.) of the end-effector is located. The position of the end-effector O_B expressed in the inertial frame N is given by $\chi = [x\ ,\ y\ ,\ z]^T$. The vector ω shows the angular velocity of the end-effector expressed in the frame attached to the end-effector. The position vectors of the i-th cable's upper and lower end-points in the inertial frame and the frame attached to the end-effector are denoted by r_{A_i} and r_{B_i} respectively. The i-th cable length vector in inertial frame is expressed as follows

$$\mathbf{q_i} = \boldsymbol{\chi} + {}^{\mathbf{N}}\mathbf{R_B}\,\mathbf{r_{B_i}} - \mathbf{r_{A_i}} \tag{1}$$

where ${}^{\mathbf{N}}\mathbf{R_B}$ is the rotation matrix of the end-effector frame with respect to the inertial frame. Considering $\mathbf{q_0}$ and $\mathbf{q_u}$ as the cable length vectors in initial and

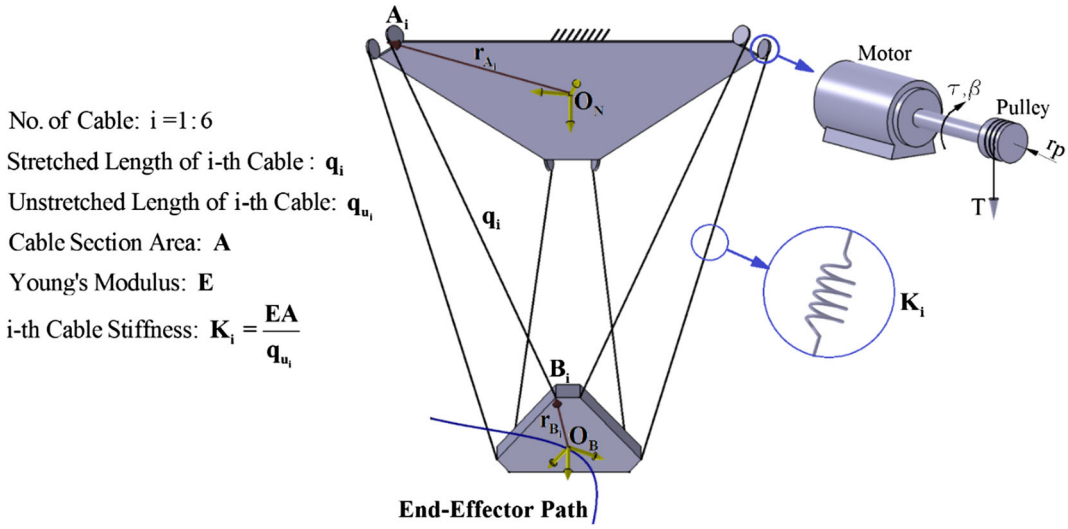

Fig. 1 Schematic picture of the 6DOF cable-suspended robot

unstretched state respectively, the following equations can be expressed

$$\mathbf{q_u} = \mathbf{q_0} - r_p \boldsymbol{\beta} \tag{2}$$

$$\Delta \mathbf{q} = \mathbf{q} - \mathbf{q_u} \tag{3}$$

$$\dot{\boldsymbol{\beta}} = -\frac{1}{r_p}\dot{\mathbf{q}}_\mathbf{u} = \frac{1}{r_p}\left(\Delta\dot{\mathbf{q}} - \dot{\mathbf{q}}\right) \tag{4}$$

where $\boldsymbol{\beta}$ denotes the rotation vector of the drums with radius r_p. The velocity vector of the end-effector, $\dot{\tilde{\mathbf{x}}}$, including the linear velocity in the inertial frame and the angular velocity in the end-effector frame, is

$$\dot{\tilde{\mathbf{x}}} = \begin{bmatrix} \dot{\boldsymbol{\chi}} \\ \boldsymbol{\omega} \end{bmatrix}, \; where: \boldsymbol{\chi} = [x\,,\; y\,,\; z]^T\,, \quad \boldsymbol{\omega} = \left[\omega_x\,,\; \omega_y\,,\; \omega_z\right]^T \tag{5}$$

The time derivative of $\mathbf{q}$ is as follows

$$\dot{\mathbf{q}} = -r_p \mathbf{A_1}\,\dot{\tilde{\mathbf{x}}} \tag{6}$$

where the matrix $\mathbf{A_1}$ is defined in the Appendix. The dynamic equations of motion can be derived using Euler-Lagrange formulation. The potential energy, kinetic energy, dissipation function and the generalized work are defined as

$$U_P = \frac{1}{2}\Delta\mathbf{q}^T\,\mathbf{K}(\mathbf{q_u})\,\Delta\mathbf{q} - m_e g\, z \quad , \quad where: \; \mathbf{K}(\mathbf{q_u}) = diag\left(\frac{EA}{\mathbf{q_u}}\right) \tag{7}$$

$$T = \frac{1}{2}\dot{\tilde{\mathbf{x}}}^T\,[\mathbf{M_e}]\,\dot{\tilde{\mathbf{x}}} + \frac{1}{2}\dot{\boldsymbol{\beta}}^T\,\mathbf{I_m}\dot{\boldsymbol{\beta}} \quad , \quad where: [\mathbf{M_e} \begin{bmatrix} m_e\,\mathbf{I_3} & \mathbf{0_3} \\ \mathbf{0_3} & \mathbf{I_e} \end{bmatrix} \tag{8}$$

$$D = \frac{1}{2}\Delta\dot{\mathbf{q}}^\mathbf{T}\mathbf{C_d}\Delta\dot{\mathbf{q}} \quad , \quad where: \mathbf{C_d}(\mathbf{q_u} = diag\left(\frac{c_d}{\mathbf{q_u}}\right) \tag{9}$$

$$W = \boldsymbol{\tau}^\mathbf{T}\,\dot{\boldsymbol{\beta}} \tag{10}$$

where E, A, c_d and $\boldsymbol{\tau}$ denote the Young's modulus of elasticity, cable section area, damping coefficient and motor torques, respectively. The end-effector mass and inertia tensor are represented by m_e and $\mathbf{I_e}$. Also, the elements of the diagonal matrix $\mathbf{I_m}$ indicate the moment of inertia of the set, consisting of the rotor, gears and the output shaft of the motors, which is expressed based on the output shaft rotation. The end-effector angular velocity can be expressed in terms of Euler angles as

$$\boldsymbol{\omega} = \boldsymbol{P}\dot{\boldsymbol{\Psi}} \quad , \quad \boldsymbol{\Psi} = [\psi, \theta, \varphi]^\mathrm{T} \tag{11}$$

Using Eq. 11, the velocity vector of the end-effector can be expressed as

$$\dot{\tilde{\mathbf{x}}} = \mathbf{A_3}\dot{\mathbf{x}} \quad , \quad \dot{\mathbf{x}} = \begin{bmatrix} \dot{\boldsymbol{\chi}}^\mathbf{T} & \dot{\boldsymbol{\Psi}}^\mathbf{T} \end{bmatrix}^\mathbf{T} \tag{12}$$

where the matrix $\mathbf{A_3}$ is given in the Appendix. Using Eqs. 7–12 and Euler-Lagrange formulation, the

dynamic equations of the cable robot with visco-elastic cables can be written as

$$\mathbf{M}\ddot{\boldsymbol{\zeta}} + \mathbf{C}(\boldsymbol{\zeta}, \dot{\boldsymbol{\zeta}}) + \mathbf{G} = \begin{bmatrix} \mathbf{0}_{1\times 6} & \boldsymbol{\tau}^{\mathbf{T}} \end{bmatrix}^{\mathbf{T}}, \quad \boldsymbol{\zeta} = \begin{bmatrix} \mathbf{x}^{\mathbf{T}} & \boldsymbol{\beta}^{\mathbf{T}} \end{bmatrix}^{\mathbf{T}} \tag{13}$$

where

$$\mathbf{M} = \begin{bmatrix} \mathbf{A_3}^{\mathbf{T}}[\mathbf{M_e}]\mathbf{A_3} & \mathbf{0_6} \\ \mathbf{0_6} & \mathbf{I_m} \end{bmatrix},$$

$$\mathrm{C} = \begin{bmatrix} \mathbf{A_3}^{\mathbf{T}}\left([\mathbf{M_e}]\mathbf{A_4} + \begin{bmatrix} \mathbf{0}_{3\times 1} \\ \mathbf{P}\dot{\boldsymbol{\psi}} \times \mathbf{I_e}\mathbf{P}\dot{\boldsymbol{\psi}} \end{bmatrix} - \mathbf{r_p}\mathbf{A_1}^{\mathbf{T}}(\mathbf{K}\boldsymbol{\Delta}\mathbf{q} + \mathbf{C_d}\dot{\boldsymbol{\Delta}}\mathbf{q})\right) \\ \mathrm{r_p}\,(\mathbf{K}\boldsymbol{\Delta}\mathbf{q} + \mathbf{C_d}\dot{\boldsymbol{\Delta}}\mathbf{q}) \end{bmatrix},$$

$$\mathbf{G} = \begin{bmatrix} \mathbf{0_{2\times 1}} \\ -m_e \mathrm{g} \\ \mathbf{0_{9\times 1}} \end{bmatrix}$$

In the case of rigid cables, $\mathbf{q} = \mathbf{q_u}$, Eq. 13 becomes

$$\bar{\mathbf{M}}\ddot{\mathbf{x}} + \bar{\mathbf{C}} + \bar{\mathbf{G}} = \bar{\mathbf{F}}\boldsymbol{\tau} \tag{14}$$

where

$$\bar{\mathbf{M}} = \mathbf{A_3}^{\mathbf{T}}\left([\mathbf{M_e}] + \mathbf{A_1}^{\mathbf{T}}\mathbf{I_m}\mathbf{A_1}\right)\mathbf{A_3},$$

$$\bar{\mathbf{G}} = \mathbf{A_3}^{\mathbf{T}}\begin{bmatrix} \mathbf{0_{2\times 1}} \\ -\mathrm{m_e g} \\ \mathbf{0_{3\times 1}} \end{bmatrix}, \quad \bar{\mathbf{F}} = \mathbf{A_3}^{\mathbf{T}}\mathbf{A_1}^{\mathbf{T}}$$

$$\bar{\mathbf{C}} = \mathbf{A_3}^{\mathbf{T}}\left([\mathbf{M_e}]\mathbf{A_4} + \begin{bmatrix} \mathbf{0_{3\times 1}} \\ \mathbf{P}\dot{\boldsymbol{\psi}} \times \mathbf{I_e}\mathbf{P}\dot{\boldsymbol{\psi}} \end{bmatrix} + \mathbf{A_1}^{\mathbf{T}}\mathbf{I_m}\,(\mathbf{A_1}\mathbf{A_4} + \mathbf{A_2})\right)$$

The overall motion of the end-effector is composed of rigid motion and the vibrational motion caused by the cables flexibility. The natural frequencies and mode shapes of the end-effector vibration can be obtained using the following linearized dynamic equation around each point of the workspace as

$$\tilde{\mathbf{M}}\ddot{\mathbf{x}} + \tilde{\mathbf{C}}\dot{\mathbf{x}} + \tilde{\mathbf{K}}\mathbf{x} = \mathbf{0} \tag{15}$$

where the matrix $\tilde{\mathbf{C}}$ is zero in the case of undamped vibration. Considering the transient matrix of Eq. 15, the Eigen values and Eigen vectors give the natural frequencies and mode shapes of the system

$$\mathbf{A} = \begin{bmatrix} \mathbf{0} & \mathbf{I} \\ -\tilde{\mathbf{M}}^{-1}\tilde{\mathbf{K}} & -\tilde{\mathbf{M}}^{-1}\tilde{\mathbf{C}} \end{bmatrix} \tag{16}$$

$$\mathbf{A}\mathbf{z} = \boldsymbol{\lambda}\mathbf{z} \tag{17}$$

where $\mathbf{z}$ and $\boldsymbol{\lambda}$ indicate the Eigen value and Eigen vector, respectively.

3 Stability Analysis

Considering the rigid model in Eq. 14, the FL control input is as follows

$$\boldsymbol{\tau} = \bar{\mathbf{F}}^{-1}\left(\bar{\mathbf{M}}\upsilon + \bar{\mathbf{C}} + \bar{\mathbf{G}}\right) \quad , \quad \upsilon = \ddot{\mathbf{x}} + \mathbf{K_p}\mathbf{e} + \mathbf{K_d}\dot{\mathbf{e}} \tag{18}$$

where the proportional gain $\mathbf{K_p}$ and the derivative gain $\mathbf{K_d}$ are positive diagonal matrices. Substituting the nonlinear control effort, (18), in Eq. 14 results in the linearized dynamic error as

$$\ddot{\mathbf{e}} + \mathbf{K_d}\dot{\mathbf{e}} + \mathbf{K_p}\mathbf{e} = \mathbf{0} \tag{19}$$

The movement of the system only due to the rigid model is called slow dynamic, whereas the vibration caused by the flexible model is considered as fast dynamic. While the FL controller leads to a stable linearized dynamic error for the rigid system, it makes the dynamic error of the flexible system partially linearized. This dynamic error is composed of the slow dynamic due to the rigid FL controller and the nonlinear fast dynamic caused by the system flexibility. Since the stability of the closed-loop flexible system is questionable, the stability analysis should be performed. The dynamical behavior of the flexible system can be investigated by dividing the dynamic equations into the slow dynamic and fast dynamics using singular perturbation techniques. In order to express the flexible system equations in the form of singular perturbations, the fast dynamic state u and small parameter ε are defined as

$$\mathbf{u} = EA\,\boldsymbol{\Delta}\mathbf{q} \tag{20}$$

$$\varepsilon^2 = \frac{1}{EA} \tag{21}$$

In addition, it is assumed that the order of the damping coefficient, c_d, in analogous to the mass-spring-damper system, is proportional to the square root of the spring constant as

$$c_d = \frac{\alpha}{\varepsilon} \quad , \quad \alpha = O(1) \tag{22}$$

Using Eqs. 20 and 21, the angular acceleration vector of the motors is obtained as

$$\ddot{\boldsymbol{\beta}} = \frac{\varepsilon^2}{r_p}\ddot{\mathbf{u}} + \mathbf{A_1}\,\mathbf{A_3}\ddot{\mathbf{x}} + \mathbf{A_1}\,\mathbf{A_4} + \mathbf{A_2} \tag{23}$$

According to Tikhonov theory, the slow dynamic state **x**and fast dynamic state **u**can be approximated as follows

$$\begin{cases} \mathbf{x} = \mathbf{x_0}(t) + \mathbf{O}(\varepsilon) \\ \mathbf{u} = \mathbf{u_0}(t) + \boldsymbol{\delta}(\eta) + \mathbf{O}(\varepsilon) \end{cases} \tag{24}$$

where $\eta = \frac{t}{\varepsilon}$ and δ are the time scale and the variable corresponding to the fast dynamic of the system. Ignoring the higher order terms, the first and second derivatives of **u** are

$$\begin{cases} \dot{\mathbf{u}} = \dot{\mathbf{u}}_\mathbf{0} + \frac{1}{\varepsilon}\frac{\mathrm{d}\boldsymbol{\delta}}{\mathrm{d}\eta} \\ \ddot{\mathbf{u}} = \ddot{\mathbf{u}}_\mathbf{0} + \frac{1}{\varepsilon^2}\frac{\mathrm{d}^2\boldsymbol{\delta}}{\mathrm{d}\eta^2} \end{cases} \tag{25}$$

Ignoring the order ε^2 and the fast dynamics, the actuator equation, obtained from Eq. 13, can be rewritten as

$$\begin{aligned} \mathbf{u_0} + \alpha\,\varepsilon\,\dot{\mathbf{u}}_0 = \frac{\mathrm{diag}(\mathbf{q_u})}{r_p}\big(\boldsymbol{\tau} - \mathbf{I_m}\big(\mathbf{A_{1_0}}\,\mathbf{A_{3_0}}\ddot{\mathbf{x}}_\mathbf{0} \\ + \mathbf{A_{1_0}}\,\mathbf{A_{4_0}} + \mathbf{A_{2_0}}\big)\big) \end{aligned} \tag{26}$$

Substituting Eq. 26 in the actuator equation, obtained from Eq. 13, the fast dynamic equation can be expressed as

$$\frac{\mathbf{I_m}}{r_p}\frac{\mathrm{d}^2\boldsymbol{\delta}}{\mathrm{d}\eta^2} + r_p diag^{-1}(\mathbf{q_u})\left(\boldsymbol{\delta} + \alpha\,\frac{\mathrm{d}\,\boldsymbol{\delta}}{\mathrm{d}\eta}\right) = \mathbf{0} \tag{27}$$

The state space representation of Eq. 27 is as follows

$$\begin{aligned} &\begin{bmatrix} \dot{\delta} \\ \ddot{\delta} \end{bmatrix} = \begin{bmatrix} \mathbf{0} & \mathbf{1} \\ -\mathbf{K_1} & -\mathbf{K_2} \end{bmatrix}\begin{bmatrix} \boldsymbol{\delta} \\ \dot{\boldsymbol{\delta}} \end{bmatrix} \quad , \\ &\mathbf{K_1} = \frac{r_p^2 EA}{\mathbf{I_m}\,diag(\mathbf{q_u})} \quad , \quad \mathbf{K_2} = \frac{r_p^2\sqrt{EA}\alpha}{\mathbf{I_m}\,diag(\mathbf{q_u})} \end{aligned} \tag{28}$$

Using Eqs. 18, 20–23, the state space representation of the end-effector dynamic is given by

$$\begin{aligned} &\begin{bmatrix} \dot{\mathbf{e}} \\ \ddot{\mathbf{e}} \end{bmatrix} = \begin{bmatrix} \mathbf{0} & \mathbf{I} \\ -\mathbf{K_p} & -\mathbf{K_d} \end{bmatrix}\begin{bmatrix} \mathbf{e} \\ \dot{\mathbf{e}} \end{bmatrix} + \begin{bmatrix} \mathbf{0} & \mathbf{0} \\ \mathbf{C}_{\delta_\mathbf{p}} & \mathbf{C}_{\delta_\mathbf{d}} \end{bmatrix}\begin{bmatrix} \boldsymbol{\delta} \\ \dot{\boldsymbol{\delta}} \end{bmatrix}, \\ &\mathbf{C}_{\delta_\mathbf{p}} = r_p\,\bar{\mathbf{M}}^{-1}\,(\mathbf{A_1}\mathbf{A_3})^\mathbf{T}\,\mathrm{diag}^{-1}(\mathbf{q_u}), \\ &\mathbf{C}_{\delta_\mathbf{d}} = c_d\mathbf{C}_{\delta_\mathbf{p}} \end{aligned} \tag{29}$$

Equation 29 shows that the bounded nonlinear term included in the dynamic error of the closed-loop system is due to the end-effector vibration. As shown in Section 4, this fast dynamic term can be treated as a process noise in the feedback linearized system.

The stability analysis is performed with the Lyapunov candidate as

$$\begin{aligned} V = \frac{1}{2}\Big(\dot{\mathbf{e}}^\mathbf{T}\,\dot{\mathbf{e}} + \mathbf{e}^\mathbf{T}\,\mathbf{K_p}\,\mathbf{e} + \kappa\begin{bmatrix} \boldsymbol{\delta}^\mathbf{T} & \dot{\boldsymbol{\delta}}^\mathbf{T} \end{bmatrix} \\ \times \begin{bmatrix} r_p^2\left(EA + \sqrt{EA}\alpha\right)\mathbf{I} & \mathbf{I_m}\mathbf{diag}(\mathbf{q_u}) \\ \mathbf{I_m}\mathbf{diag}(\mathbf{q_u}) & \mathbf{I_m}\mathbf{diag}(\mathbf{q_u}) \end{bmatrix}\begin{bmatrix} \boldsymbol{\delta} \\ \dot{\boldsymbol{\delta}} \end{bmatrix}\Big) \end{aligned} \tag{30}$$

where $\kappa > 0$ is an arbitrary scalar. The first two terms in Eq. 30 constitute a Lyapunov function for rigid FL controller. Since all the state variables should be considered in the constructed function, the weighted quadratic form of the fast dynamic states is used in the third term of Eq. 30. The derivative of Eq. 30 becomes

$$\begin{aligned} \dot{V} = -\dot{\mathbf{e}}^\mathbf{T}\mathbf{K_d}\dot{\mathbf{e}} + \dot{\mathbf{e}}^\mathbf{T}\begin{bmatrix} \mathbf{C}_{\delta_\mathbf{p}} & \mathbf{C}_{\delta_\mathbf{d}} \end{bmatrix}\begin{bmatrix} \boldsymbol{\delta} \\ \dot{\boldsymbol{\delta}} \end{bmatrix} - \begin{bmatrix} \boldsymbol{\delta}^\mathbf{T} & \dot{\boldsymbol{\delta}}^\mathbf{T} \end{bmatrix} \\ \times \begin{bmatrix} r_p^2 EA\,\mathbf{I} & \mathbf{0} \\ \mathbf{0} & \alpha r_p^2\sqrt{EA}\,\mathbf{I} - \mathbf{I_m}\mathbf{diag}(\mathbf{q_u}) \end{bmatrix}\begin{bmatrix} \boldsymbol{\delta} \\ \dot{\boldsymbol{\delta}} \end{bmatrix} \\ + \begin{bmatrix} \boldsymbol{\delta}^\mathbf{T} & \dot{\boldsymbol{\delta}}^\mathbf{T} \end{bmatrix}\begin{bmatrix} \mathbf{0} & \mathbf{I_m}\mathbf{diag}(\dot{\mathbf{q}}_\mathbf{u}) \\ \mathbf{I_m}\mathbf{diag}(\dot{\mathbf{q}}_\mathbf{u}) & \mathbf{I_m}\mathbf{diag}(\dot{\mathbf{q}}_\mathbf{u}) \end{bmatrix}\begin{bmatrix} \boldsymbol{\delta} \\ \dot{\boldsymbol{\delta}} \end{bmatrix} \end{aligned} \tag{31}$$

The system stability can be shown by obtaining the necessary conditions to make $\dot{V}$ negative semi-definite. To this end, the upper bound of the terms included in Eq. 31 should be specified. Considering the smallest Eigen value of the positive definite matrix $\mathbf{K_d}$, the upper bound of the first term is

$$-\dot{\mathbf{e}}^\mathbf{T}\mathbf{K_d}\dot{\mathbf{e}} \le -\lambda_{\min}(\mathbf{K_d})\,\|\dot{\mathbf{e}}\| = -\lambda_{md}\,\|\dot{\mathbf{e}}\|^2 \tag{32}$$

Indicating the maximum singular value of a matrix by $\sigma_{\max}(.)$, the upper bound of the second term is obtained as

$$\begin{aligned} \dot{\mathbf{e}}^\mathbf{T}\begin{bmatrix} \mathbf{C}_{\delta_\mathbf{p}} & \mathbf{C}_{\delta_\mathbf{d}} \end{bmatrix}\begin{bmatrix} \boldsymbol{\delta} \\ \dot{\boldsymbol{\delta}} \end{bmatrix} &\le \|\dot{\mathbf{e}}\|\left\|\begin{bmatrix} \boldsymbol{\delta} \\ \dot{\boldsymbol{\delta}} \end{bmatrix}\right\|\sigma_{\max}\left(\begin{bmatrix} \mathbf{C}_{\delta_\mathbf{p}} & \mathbf{C}_{\delta_\mathbf{d}} \end{bmatrix}\right) \\ &= \sigma_{me}\,\|\dot{\mathbf{e}}\|\left\|\begin{bmatrix} \boldsymbol{\delta} \\ \dot{\boldsymbol{\delta}} \end{bmatrix}\right\| \end{aligned} \tag{33}$$

Since $q_{u_i}(t) > 0, \quad i = 1..6$ always holds during the operation, assuming the following condition

$$c_d > \frac{\mathbf{I_m}}{r_p^2}\max\left(q_{u_i}(t)\right) \tag{34}$$

gives the upper bound of the third term in Eq. 31 as

$$
\begin{aligned}
&-\kappa \begin{bmatrix} \boldsymbol{\delta} \\ \dot{\boldsymbol{\delta}} \end{bmatrix}^{\mathbf{T}} \begin{bmatrix} r_p^2 EA\,\mathbf{I} & \mathbf{0} \\ \mathbf{0} & r_p^2 c_d\,\mathbf{I} - \mathbf{I_m diag(q_u)} \end{bmatrix} \begin{bmatrix} \boldsymbol{\delta} \\ \dot{\boldsymbol{\delta}} \end{bmatrix} \\
&\leq -\kappa \lambda_{\min} \left(\begin{bmatrix} r_p^2 EA\,\mathbf{I} & \mathbf{0} \\ \mathbf{0} & r_p^2 c_d\,\mathbf{I} - \mathbf{I_m diag(q_u)} \end{bmatrix} \right) \\
&\quad \times \left\| \begin{bmatrix} \boldsymbol{\delta} \\ \dot{\boldsymbol{\delta}} \end{bmatrix} \right\|^2 = -\kappa \lambda_{m\delta} \left\| \begin{bmatrix} \boldsymbol{\delta} \\ \dot{\boldsymbol{\delta}} \end{bmatrix} \right\|^2 \quad , \quad \lambda_{m\delta} > 0 \qquad (35)
\end{aligned}
$$

The vector of cable length rate, $\dot{\mathbf{q}}_\mathbf{u}$, depends on the motor shaft speed, $\dot{\boldsymbol{\beta}}$. Therefore, considering the maximum allowable motor speed, denoted by $\omega > 0$, the last term in Eq. 31 has the following upper bound

$$
\begin{aligned}
&\begin{bmatrix} \boldsymbol{\delta}^{\mathbf{T}} & \dot{\boldsymbol{\delta}}^{\mathbf{T}} \end{bmatrix} \begin{bmatrix} \mathbf{0} & \mathbf{I_m diag}(\dot{\mathbf{q}}_\mathbf{u}) \\ \mathbf{I_m diag}(\dot{\mathbf{q}}_\mathbf{u}) & \mathbf{I_m diag}(\dot{\mathbf{q}}_\mathbf{u}) \end{bmatrix} \begin{bmatrix} \boldsymbol{\delta} \\ \dot{\boldsymbol{\delta}} \end{bmatrix} \\
&\quad \leq \left\| \begin{bmatrix} \boldsymbol{\delta} \\ \dot{\boldsymbol{\delta}} \end{bmatrix} \right\|^2 \sigma_{\max} \left(\begin{bmatrix} \mathbf{0} & \mathbf{I_m} r_p \omega \\ \mathbf{I_m} r_p \omega & \mathbf{I_m} r_p \omega \end{bmatrix} \right) \\
&\quad = \sigma_{mq} \left\| \begin{bmatrix} \boldsymbol{\delta} \\ \dot{\boldsymbol{\delta}} \end{bmatrix} \right\|^2 \qquad (36)
\end{aligned}
$$

As a result the upper bound of $\dot{V}$ is obtained as

$$
\begin{aligned}
\dot{V} \leq &-\begin{bmatrix} \|\dot{\mathbf{e}}\| & \left\| \begin{bmatrix} \boldsymbol{\delta} \\ \dot{\boldsymbol{\delta}} \end{bmatrix} \right\| \end{bmatrix} \begin{bmatrix} \lambda_{md} & -\frac{\sigma_{me}}{2} \\ -\frac{\sigma_{me}}{2} & \kappa\lambda_{m\delta} - \sigma_{mq} \end{bmatrix} \\
&\times \begin{bmatrix} \|\dot{\mathbf{e}}\| \\ \left\| \begin{bmatrix} \boldsymbol{\delta} \\ \dot{\boldsymbol{\delta}} \end{bmatrix} \right\| \end{bmatrix} \qquad (37)
\end{aligned}
$$

In order to hold $\dot{V} \leq 0$, the following conditions should be satisfied

$$
\lambda_{md} \geq \frac{\sigma_m^2}{4(\kappa\lambda_{m\delta} - \sigma_{mq})} \qquad (38)
$$

$$
\lambda_{m\delta} > \frac{\sigma_{mq}}{\kappa} \qquad (39)
$$

Since the arbitrary scalar κ can be chosen large enough to fulfill the conditions (38) and (39), the derivative gain, $\mathbf{K_d}$, only needs to be positive definite. Therefore, Eq. 34 and positive definiteness of the derivative gain matrix are the only required conditions to guarantee the system stability.

4 LQG Control Law in Presence of Noise

In Section 3, it is proved that a certain condition for the damping coefficient ensures the stability of the closed-loop dynamic of the flexible system. This condition can be more relaxed by considering the fast dynamic term in Eq. 29 as a process noise and filtering that using the LQG approach. The LQG control method is indeed LQR controller where the states used in the control input are estimated using Kalman filter. Considering Eqs. 18 and 29, the state space representation of the system can be expressed as follows

$$
\begin{aligned}
&\begin{cases} \dot{\xi} = \mathbf{A}\xi + \mathbf{B}\upsilon + \mathbf{w} \\ \mathbf{y} = \mathbf{C}\xi + \mathbf{v} \end{cases} \quad , \quad \xi = \begin{bmatrix} \mathbf{x} \\ \dot{\mathbf{x}} \end{bmatrix} \quad , \\
&\mathbf{A} = \begin{bmatrix} \mathbf{0} & \mathbf{I} \\ \mathbf{0} & \mathbf{0} \end{bmatrix} \quad , \quad \mathbf{B} = \begin{bmatrix} \mathbf{0} \\ \mathbf{I} \end{bmatrix} \quad , \quad \mathbf{C} = \mathbf{I} \qquad (40)
\end{aligned}
$$

where $\mathbf{y}$ denotes the system output. The uncorrelated zero mean vectors $\mathbf{w}(t)$ and $\mathbf{v}(t)$ represent the process and measurement noise, respectively. Also, the pair $(\mathbf{A}, \mathbf{C})$ is observable. Considering fulfillment of condition (34), no restriction is needed for the control gains. Therefore, ignoring the process and measurement noise, the optimal gains can be obtained using LQR method by minimizing the cost function given by

$$
\begin{aligned}
&J = \int_0^\infty [\boldsymbol{\zeta}^T \mathbf{Q} \boldsymbol{\zeta} + \mathbf{u}^T \mathbf{R} \mathbf{u}] dt \quad , \quad \boldsymbol{\zeta} = \begin{bmatrix} \mathbf{e} \\ \dot{\mathbf{e}} \end{bmatrix} \quad , \\
&\mathbf{u} = -\begin{bmatrix} \mathbf{K_p} & \mathbf{K_d} \end{bmatrix} \boldsymbol{\zeta} \qquad (41)
\end{aligned}
$$

where $\mathbf{Q}$ and $\mathbf{R}$ are positive and semi-positive definite matrix, respectively. Therefore, the control gains are determined considering a trade-off between the system error and the control input of the outer loop. The weighting matrices Q and R in Eq. 41 are used to penalize the errors and the control input. Using the Bryson's rule [19], the diagonal elements of the weight matrices can be determined as follows:

$$
\begin{aligned}
&\mathbf{Q} = \operatorname{diag}\left(\cdots, \frac{1}{\max(\xi_i^2)}, \cdots \right) \quad , \\
&\mathbf{R} = \rho \operatorname{diag}\left(\cdots, \frac{1}{\max(u_j^2)}, \cdots \right) \qquad (42)
\end{aligned}
$$

where ρ gives the relative weighting between the control input and state error. Although the Bryson's rule usually gives good results, it can be considered as a starting point to a trial-and-error aimed at obtaining desirable time performance of the closed-loop system. The initial diagonal elements of the weighting matrices can be tuned so that it meets some additional time

optimality criteria in terms of overshoot, rise and settling time, etc. In this regard, some researchers, as in [20, 21], employed genetic algorithm to find out the weighting matrices considering time domain criteria. However, in this paper the weighting matrices are determined only based on the Bryson's rule. Next, the optimal gains of the FL controller are obtained as follows

$$\left[\mathbf{K_p}\ \mathbf{K_d}\right]_{\mathbf{opt}} = \mathbf{R}^{-1}\mathbf{B}^T\mathbf{P} \tag{43}$$

where the matrix $\mathbf{P}$ is the solution of the algebraic Riccati equation

$$\mathbf{A}^T\mathbf{P} + \mathbf{PA} + \mathbf{Q} - \mathbf{PBR}^{-1}\mathbf{B}^T\mathbf{P} = \mathbf{0} \tag{44}$$

Considering the covariance of the measurement and process noise as

$$\begin{cases} \bar{\mathbf{Q}} = E\left(\mathbf{w}\mathbf{w}^T\right) \\ \bar{\mathbf{R}} = E\left(\mathbf{v}\mathbf{v}^T\right) \end{cases} \tag{45}$$

the control input can be computed using the estimated state, obtained by solving the following equation

$$\dot{\hat{\boldsymbol{\xi}}} = \mathbf{A}\hat{\boldsymbol{\xi}} + \mathbf{B}\upsilon + \mathbf{L}(\mathbf{y} - \mathbf{C}\hat{\boldsymbol{\xi}}) \tag{46}$$

The filter gain $\mathbf{L}$ is determined as follows

$$\mathbf{L} = \bar{\mathbf{P}}\mathbf{C}^T\bar{\mathbf{R}}^{-1} \tag{47}$$

where the matrix $\bar{\mathbf{P}}$ is the solution of the Riccati equation

$$\mathbf{A}^T\bar{\mathbf{P}} + \bar{\mathbf{P}}\mathbf{A} + \bar{\mathbf{Q}} - \bar{\mathbf{P}}\mathbf{B}\bar{\mathbf{R}}^{-1}\mathbf{B}^T\bar{\mathbf{P}} = \mathbf{0} \tag{48}$$

5 Simulation

In general, the number of cables of an n-DOF cable robot must be equal to or larger than n + 1 to satisfy the force-closure condition. In fully-constrained cable robots, where the number of cables exceeds the number of DOF, the cables tension can be specified for a given end-effector pose by calculating the null space of the Jacobian matrix. An under-constrained cable robot satisfies the force-closure condition if the gravity is large enough to be dealt as a special cable [22], otherwise the end-effector trajectory should be redesigned. However, in both types of the cable robots determining the force-closure workspace can help the trajectory planning [23]. In this paper, the end-effector trajectories are specified such that the positive cable tension condition holds.

The simulations are performed using the dynamical and geometrical parameters provided in Table 1. The cable end points are located on the corners of the triangular end-effector and platform. In the first simulation, a frequency analysis around each point in the workspace is performed. Existence of measurement noise together with the fast dynamic movement can lead to the system instability. Therefore, in the second simulation, the effectiveness of the LQG controller compared with the SMC method used in [7] as well as the LQR controller, in the presence of measurement noise, is demonstrated. In order to show improvement of the system stability condition, the

Table 1 Geometrical parameters

Name	Symbol	Value	Unit
Side length of the triangular plate of the platform	–	1.19	m
Side length of the triangular end-effector	–	0.17	m
Radius of the cable drums	r	0.015	m
End-effector mass	m_e	3.1	kg
Equivalent moment of inertia of the motors	$\mathbf{I_m}$	0.003 $\mathbf{I_6}$	kg.m^2
Moment of inertia tensor of the end-effector	$\mathbf{I_e}$	diag(0.0018, 0.0018, 0.0037)	kg.m^2

third simulation compares performance of the LQR and LQG controllers while the minimum damping condition is violated. Finally, the effect of modulus of elasticity and damping coefficient on the cables tension and position error is investigated in the fourth simulation.

5.1 Frequency Analysis

Considering Eqs. 16–17, six frequencies and damping ratios are obtained for each point in the workspace. By changing the mass matrix and observing the variation in the frequencies, it is found that these values can be divided into four modes. This is due to the significant interaction between horizontal coordinates, x and y, and the first two Euler angle coordinates, ψ and θ. The modes are named as translational mode along vertical axis z, translational mode along horizontal axes x and y, angular mode around vertical axis φ and angular mode around horizontal axes ψ and θ. The end-effector vibration is a weighted combination of these modes.

A frequency analysis considering EA = 15000 and cd = 20 is performed. As shown in Figs. 2 and 3, near the height Z = 0.8 m, a peak value for the frequency and damping ratio in the vertical translational mode is reached. On the other hand, for translational mode along horizontal axes, increase in Z, i.e. increase in the distance between the upper plate and the end-effector, decreases the frequencies and damping ratios.

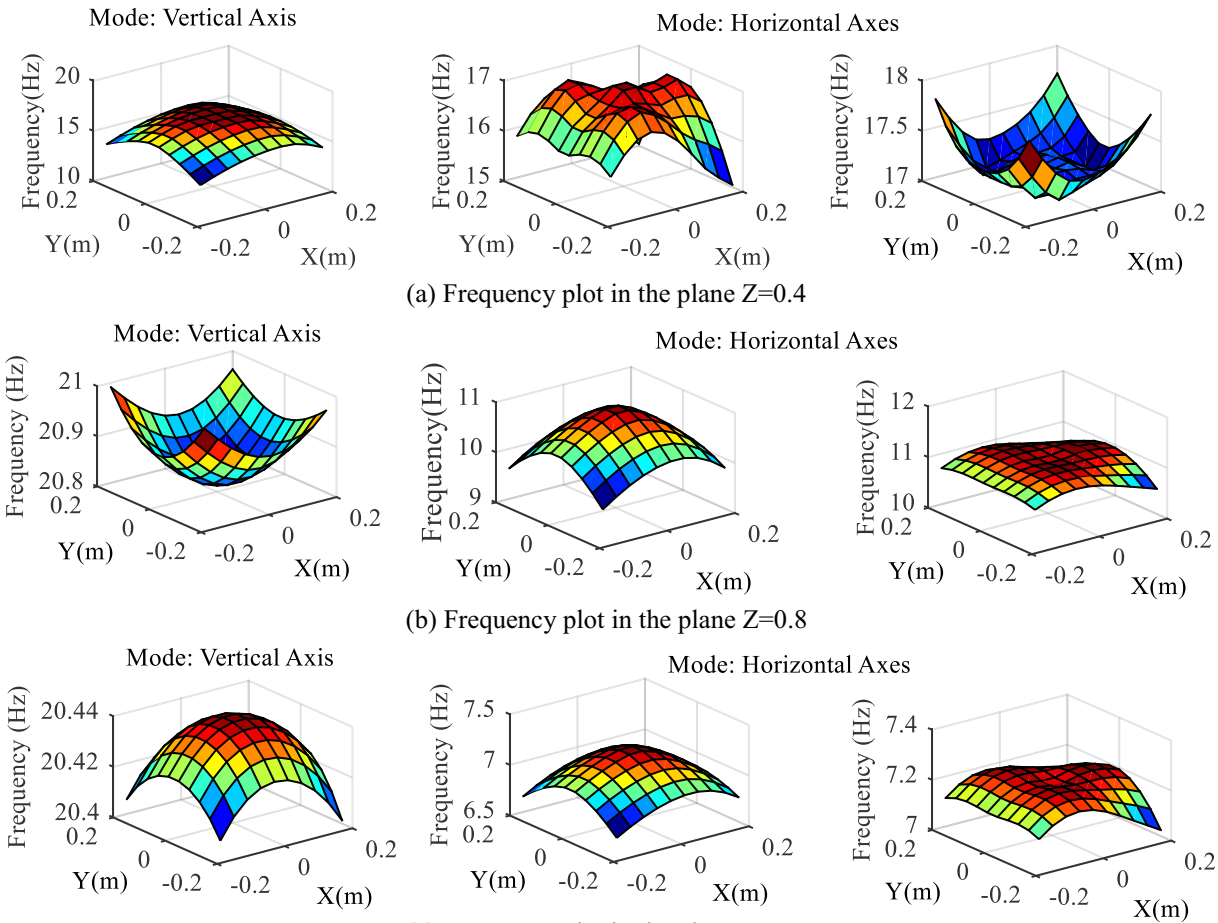

Fig. 2 Frequencies of translational mode

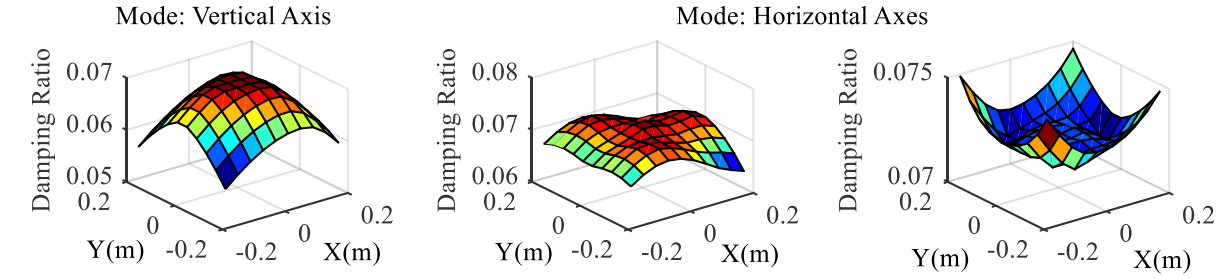

(a) Damping ratio plot in the plane Z=0.4

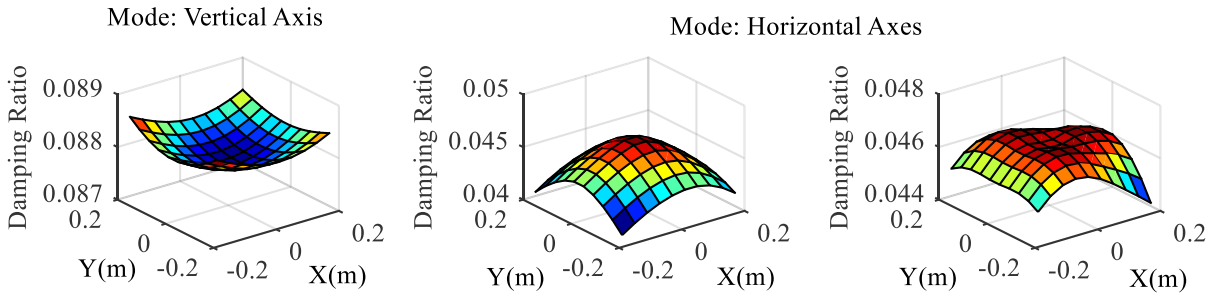

(b) Damping ratio plot in the plane Z=0.8

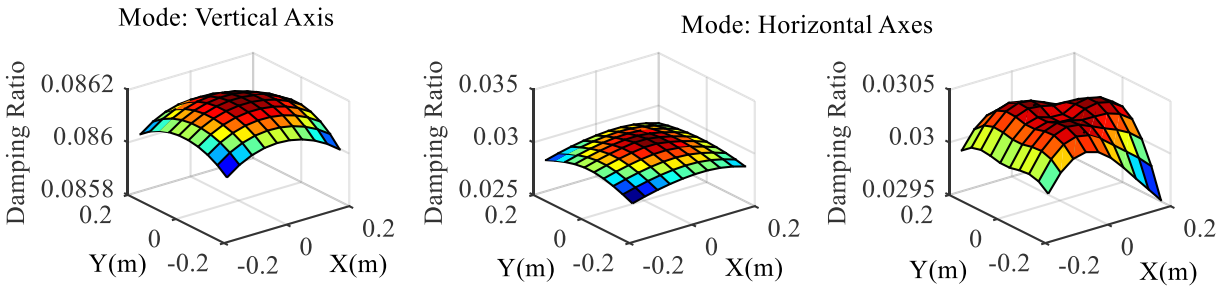

(c) Damping ratio plot in the plane Z=1.2

Fig. 3 Damping ratio of translational mode

According to Figs. 4, 5, the angular vibrations have larger damping ratios and frequencies, in comparison with the translational mode vibrations. This implies that the vibratory response in the horizontally orientated state of the end-effector is more dominated by the translational modes. In practice, knowing the damping and frequency modes in the workspace can help to predict or reduce the vibrations by appropriate trajectory planning.

5.2 Comparative Simulation I

In order to investigate the effective performance of the LQG controller in comparison with the LQR as well as the SMC method in [7] in presence of measurement noise, a simulation is performed. The desired trajectory is considered as follows

$$\mathbf{x} = \left[0.2\sin\left(\frac{2\pi t}{10}\right) \quad 0.2\cos\left(\frac{2\pi t}{10}\right) \quad 1 + 0.05\sin\left(\frac{2\pi t}{2}\right) \quad \mathbf{0}_{1\times 3}\right]^T \tag{49}$$

The initial pose of the end-effector is

$$\mathbf{x_0} = [0.02, 0.22, 1.05, 0, 0, 0]^T \tag{50}$$

The end-effector velocity at the start point is zero. A zero-mean noise with the normal distribution and

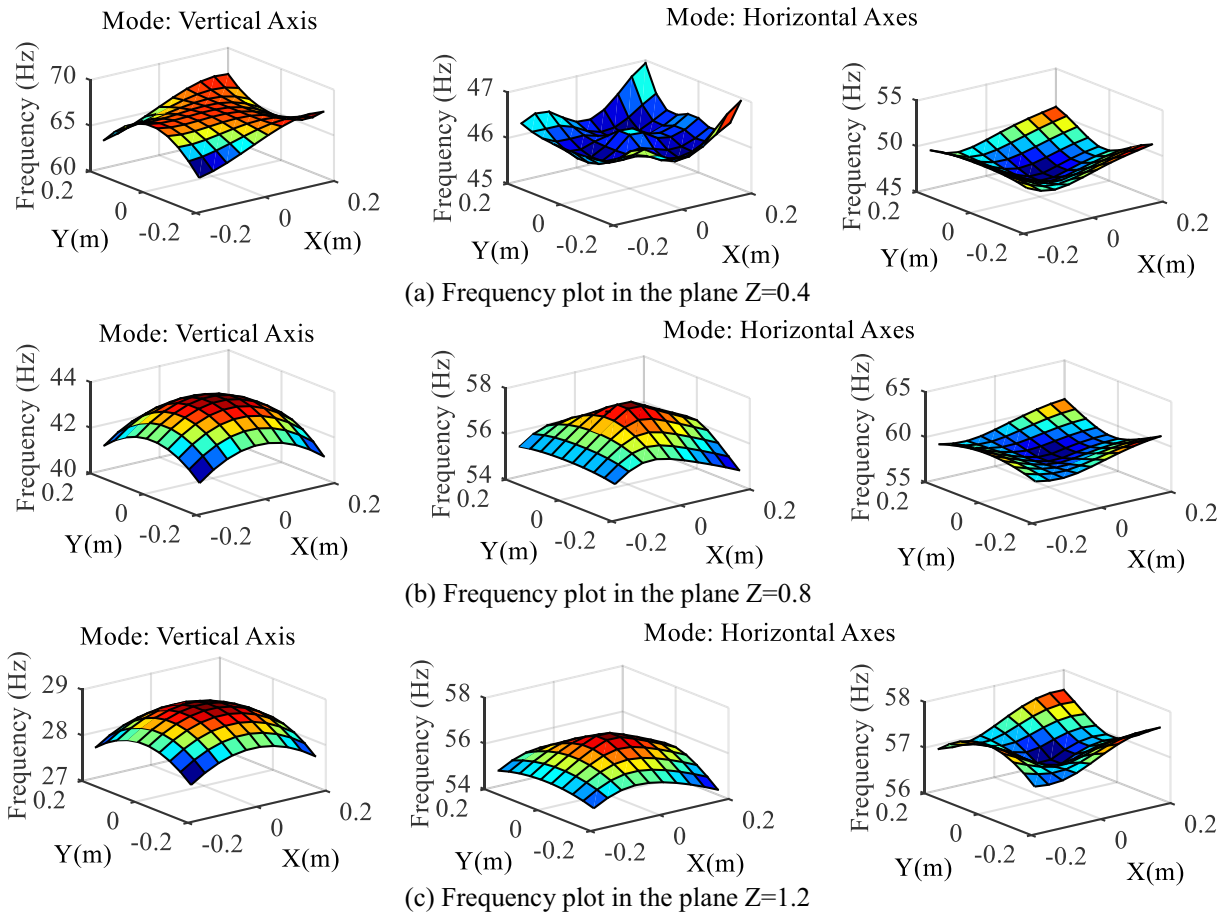

Fig. 4 Frequencies of angular mode

the following standard deviation is added to the measurement output

$$\sigma_{\mathbf{n}} = \left[\, 0.006\mathbf{I_3}\ 0.002\mathbf{I_6}\ 0.01\mathbf{I_3} \,\right]^T \tag{51}$$

The sliding surface of the SMC controller is considered as follows

$$\mathbf{s} = \dot{\mathbf{e}} + 11.8\mathbf{e} \tag{52}$$

In order to avoid chattering, the function "tanh(s)" is employed instead of "Sgn(s)". The control gain of the SMC is considered as

$$\mathbf{K} = \text{diag}(1.4, 1.4, 1.4, 3.5, 3.5, 3.5) \tag{53}$$

The weighting matrices used in the LQR and LQG methods are obtained using Eq. 42 and the maximum value of the errors and control input of the outer loop

$$\begin{aligned} \max(\text{error}) = \Big[& (0.05, 0.05, 0.05)\,\text{m}\ (3, 3, 3)\,\text{deg} \\ & \times (0.01, 0.01, 0.01)\,\frac{\text{m}}{s} \\ & \times (0.6, 0.6, 0.6)\,\frac{\text{deg}}{s} \Big] \\ \max(\text{input}) = \Big[& (1, 1, 1)\,\tfrac{\text{m}}{s^2}\ (1,\ 1,\ 1)\,\tfrac{\text{rad}}{s^2} \Big],\ \rho = 1 \end{aligned} \tag{54}$$

The cable properties and the covariance matrices used in the LQG controller are provided in Table 2, in SI units.

As shown in Figs. 6 and 7, simulation with both approaches, i.e. LQR and SMC, stops due to the

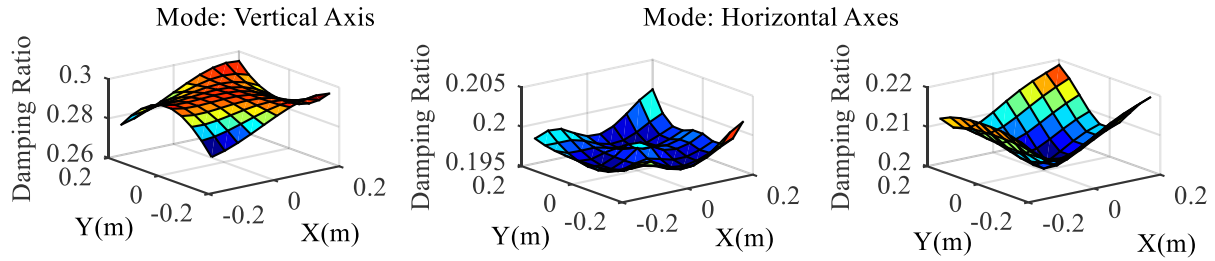

(a) Damping ratio plot in the plane Z=0.4

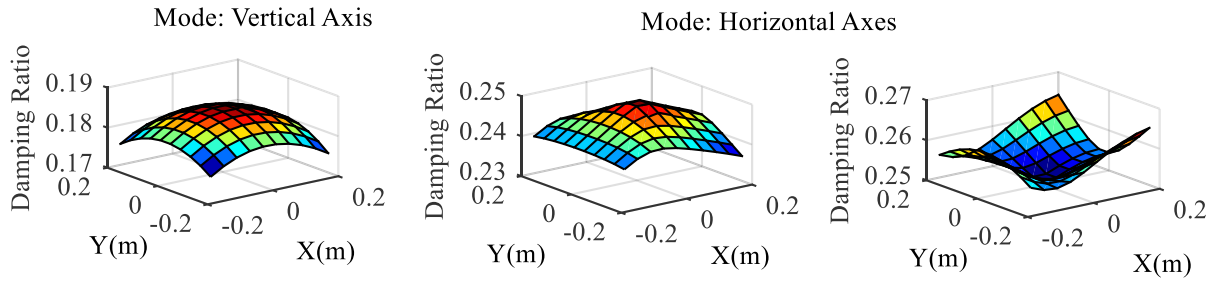

(b) Damping ratio plot in the plane Z=0.8

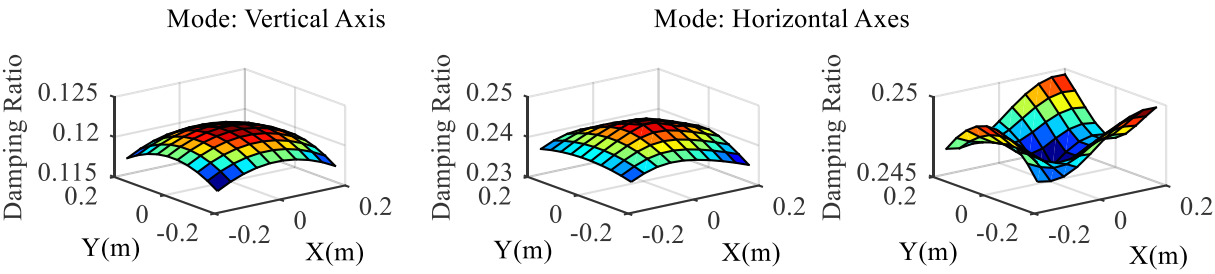

(c) Damping ratio plot in the plane Z=1.2

Fig. 5 Damping ratio of angular mode

cumulative errors, caused by the measurement noise. Figure 8 shows failure of the tracking. As illustrated in Figs. 9 and 10, both of the control inputs have diverged and resulted in the system instability.

Employing the LQG approach, the tracking is performed effectively. Figures 11 and 12 show the tracked trajectory of the end-effector in comparison with the desired and estimated trajectories. Figure 13 shows that the position error has decreased from 57 mm at the start point to below 1.5 mm. In addition, according to Fig. 14 the norm of the Euler angle errors has not exceeded 0.09deg. The control input is demonstrated in Fig. 15. Due to the difference between the

Table 2 Simulation parameters

Name	Symbol	Value
Cable stiffness	EA	15000
Damping coefficient	c_d	20
Covariance matrix of measurement noise	$\bar{\mathbf{Q}}$	1e-3 $\mathbf{I_{12}}$
Covariance matrix of process noise	$\bar{\mathbf{R}}$	1e-5 $\mathbf{I_{12}}$

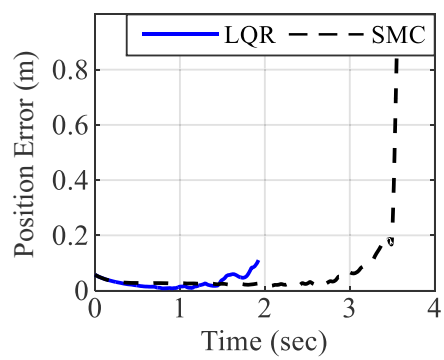

Fig. 6 Position error

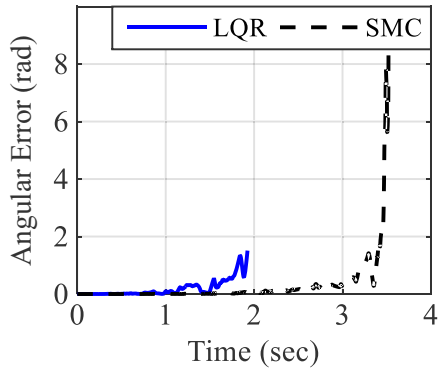

Fig. 7 Norm of Euler angle errors

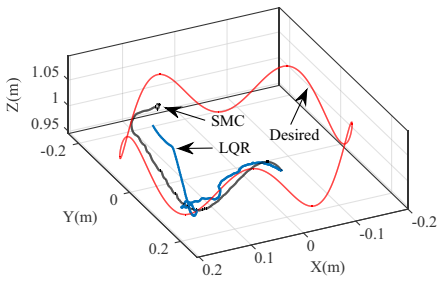

Fig. 8 Tracking failure

actual and desired initial velocity of the end-effector, a damped tension oscillation can be observed in Fig. 16.

5.3 Comparative Simulation II

Considering Eq. 34, the minimum value of c_d =13.3 is needed to guarantee the stability of the system. In the case of lower damping, the tension oscillation induced by the internal dynamics can increase and lead to the system instability. The second term in the right side of Eq. 29 can be considered as a process noise, produced by the system flexibility, added to the linearized close loop system. Therefore, the LQG approach should act more effectively in comparison with the LQR method where the noise compensation is not taken into account. This matter is verified by simulation with damping coefficient of c_d =10, i.e. lower than the given value for the guaranteed stability. The trajectory considered in this simulation is as follows

$$\mathbf{x}=\begin{cases}\left[-0.1+0.2\frac{t}{2.5}\ \ -0.1\ \ 0.6\ \ \mathbf{0}_{1\times 3}\right]^T, t\in[0,2.5]\\ \left[0.1\ \ -0.1+0.2\frac{t-2.5}{2.5}\ \ 0.6\ \ \mathbf{0}_{1\times 3}\right]^T, t\in[2.5,5]\\ \left[0.1-0.2\frac{t-5}{2.5}\ \ 0.1\ \ 0.6\ \ \mathbf{0}_{1\times 3}\right]^T, t\in[5,7.5]\\ \left[-0.1\ \ 0.1-0.2\frac{t-7.5}{2.5}\ \ 0.6\ \ \mathbf{0}_{1\times 3}\right]^T, t\in[7.5,10]\end{cases} \quad (55)$$

The initial pose of the end-effector is

$$\mathbf{x_0}=[-0.08,-0.08,0.65,0,0,0]^T \quad (56)$$

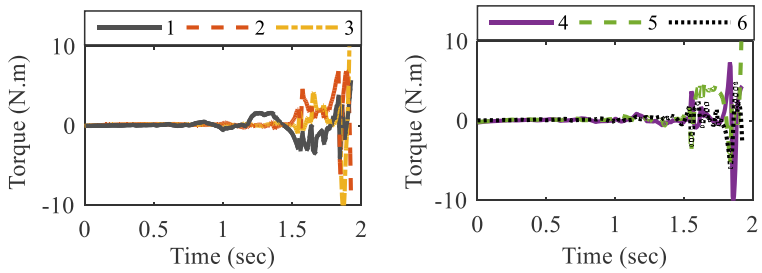

(a) 1st, 2nd and 3rd motor (b) 4th, 5th and 6th motor

Fig. 9 Control input with LQR method

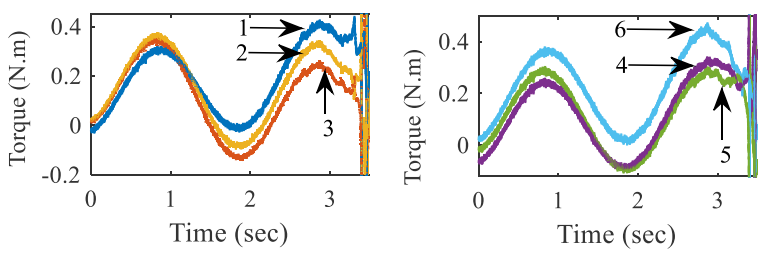

(a) 1st, 2nd and 3rd motor (b) 4th, 5th and 6th motor

Fig. 10 Control input with SMC method

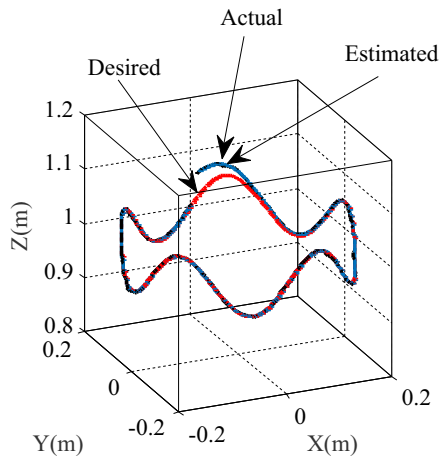

Fig. 11 Trajectory with LQG method

The rest of the parameters are according to Table 2. Simulation using LQR method shows that the system becomes unstable. As illustrated in Figs. 17, the end-effector cannot converge to the desired trajectory. However, using LQG controller the end-effector approaches to the desired trajectory, (Fig. 18). Figure 19 demonstrates the precise convergence in Z direction. According to Fig. 20, the position error decreases from 0.66m at initial position to below 8 mm. In addition, Fig. 21 indicates that during the simulation, the angular error is remained below 1.5e-3 rad. Since the desired trajectory is square, an overshoot is seen in the sharp corners of the path. This is also observable in the control input, Fig. 22. The sudden changes in the control input causes a damped oscillation of cable tension (Fig. 23).

5.4 Comparative Simulation II

In order to demonstrate the effect of cable elasticity and damping coefficient on the end-effector vibration

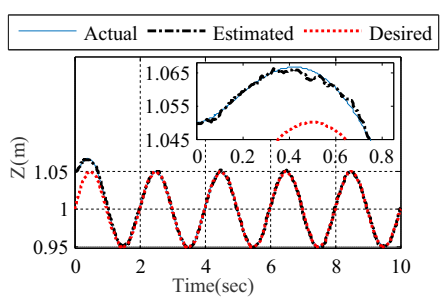

Fig. 12 Trajectory in Z direction with LQG method

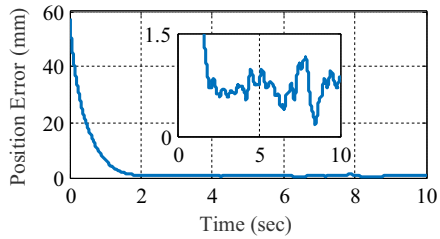

Fig. 13 Position error with LQG method

and tension oscillation, four simulations considering EA = 2000, 15000 and c_d = 8, 20 are performed. The desired trajectory and the rest of parameters are similar to the previous simulation. Figures 24 and 25 show that vibration amplitude increases with decrease of cable stiffness, and decreases with increase of damping coefficient and cable stiffness. As shown in Figs. 26, 27, this result can also be observed in the tension oscillation.

Since the sudden changes in the desired trajectory is in the horizontal plane, the translational mode along horizontal axes x and y seems to be dominant during the simulation. Furthermore, based on the workspace analysis for EA = 15000 and c_d = 20, in Section 5.1, the damping ratio in the mentioned mode has the lowest value, which in turn further supports the dominance of this mode. According to Fig. 27, the vibration frequency considering EA = 15000 and c_d = 20 is about 15 Hz, which is identical with the value obtained for z = 0.6 m by interpolation between the second and third columns of Fig. 2a–b.

6 Experimental Verification

Verification of the approach presented in this paper is performed using a 6-dof cable-suspended robot

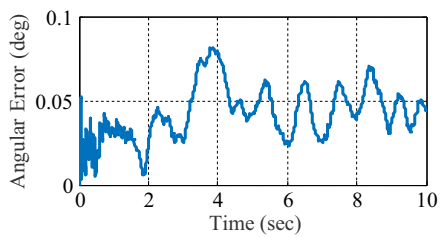

Fig. 14 Norm of Euler angle errors with LQG method

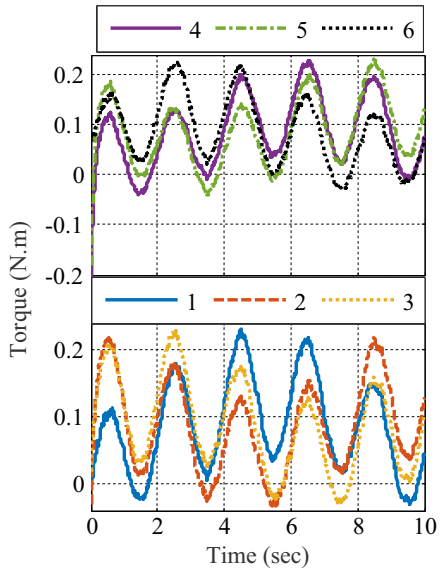

Fig. 15 Control input with LQG method

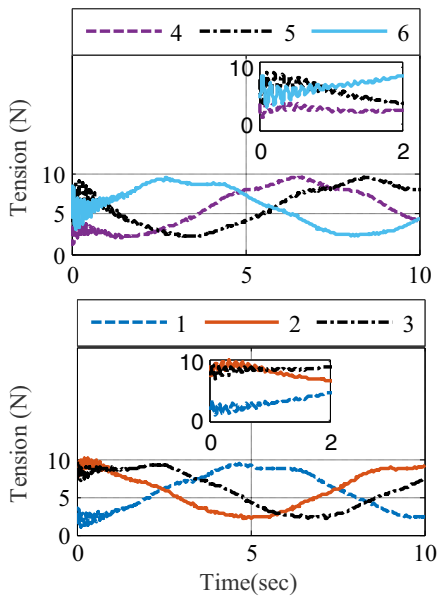

Fig. 16 Tension with LQG method

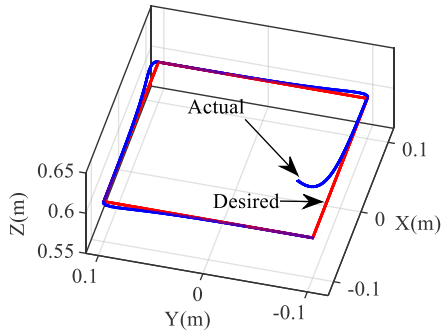

Fig. 18 Tracking with LQG method

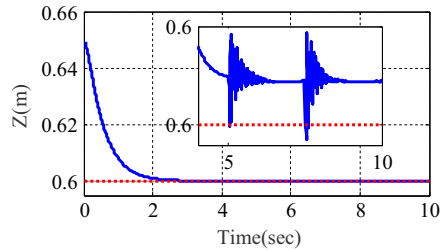

Fig. 19 Trajectory in Z direction with LQG method

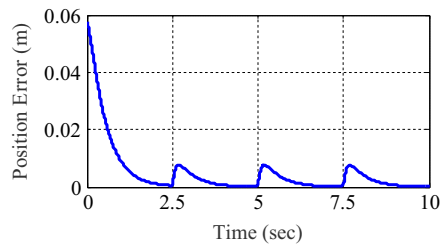

Fig. 20 Position error with LQG method

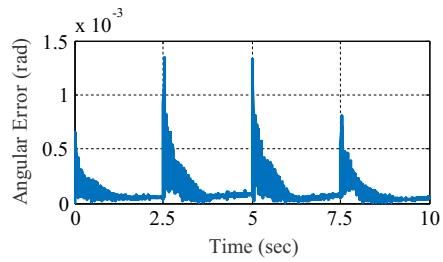

Fig. 21 Norm of Euler angle errors with LQG method

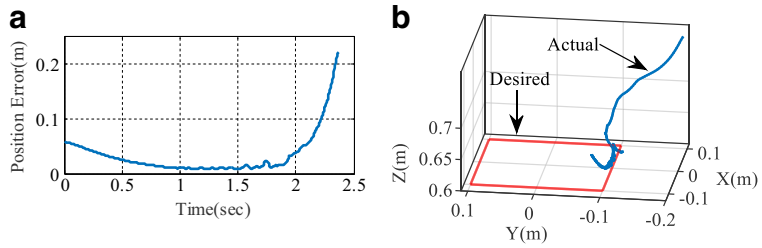

Fig. 17 **a** Position error with LQR method. **b** Tracking failure with LQR method

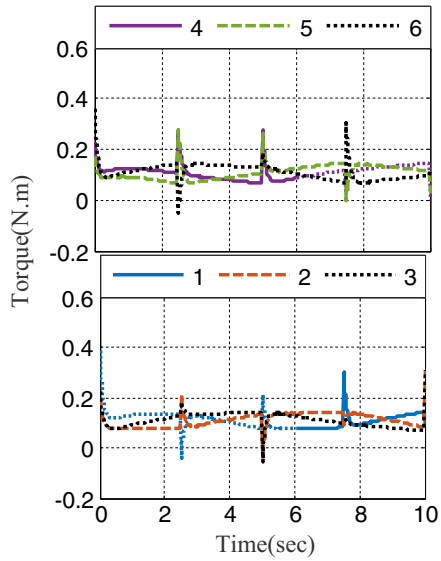

Fig. 22 Control input with LQG method

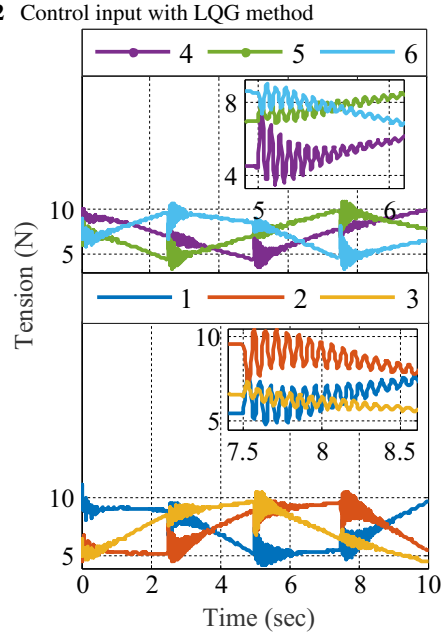

Fig. 23 Tension with LQG method

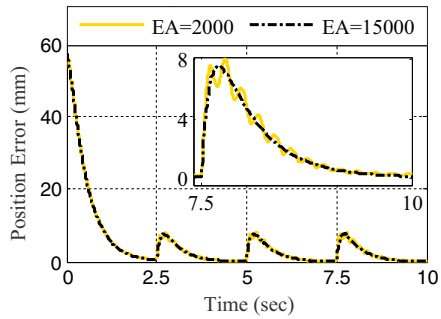

Fig. 24 Position error with c_d =8

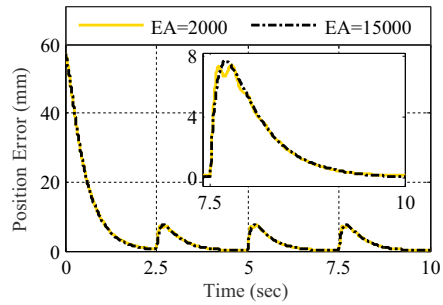

Fig. 25 Position error with c_d =20

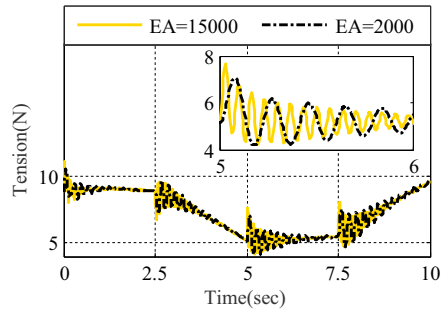

Fig. 26 Tension of the 1st cable with c_d =8

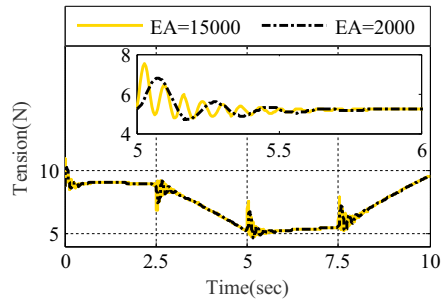

Fig. 27 Tension of the 1st cable with c_d =20

Fig. 28 ICastBot

Table 3 Motor Specifications

Name	Symbol	Value	Unit
Stall torque of the platform motors	$\tau_{\theta_{Stall}}$	45.17	N.m
Stall torque of the CDPR motors	$\tau_{\beta_{Stall}}$	2.074	N.m
No load speed of the platform motors	$\dot{\theta}_{NoLoad}$	102	rpm
No load speed of the CDPR motors	$\dot{\beta}_{NoLoad}$	250	rpm

manufactured in the robotic lab of Iran University of Science and Technology, ICasBot (Fig. 28). The cables of ICasBot are driven by PMDC motors. The parameters of the motors are according to Table 3. The rest of the robot specifications have been provided in Table 1. The position feedback of the end-effector is provided using the incremental encoders installed on the motor output shaft and direct kinematics. The implementation of the control law is performed in Matlab software, where the calculated control efforts are converted to the voltage values. These values are then applied to the motors through PIC microcontrollers and motor drivers.

The test is performed considering a spiral trajectory as follows

$$\mathbf{x} = \left[\, 0.05\sin(t) \;\; 0.05\cos(t) \;\; 0.8 - 0.032t \;\; \mathbf{0}_{1\times 3} \,\right]^T \quad (57)$$

Figures 29 and 30 show the trajectory tracking of the end-effector in XYZ and Z direction, respectively. According to the figures, the overall motion resulted from the experimental results matches well with the desired trajectory. The total trajectory length tracked by the end-effector is L = 593.6 mm. As shown in Fig. 31, the maximum position error of the experiment

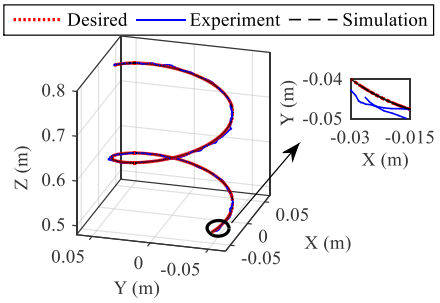

Fig. 29 The end-effector trajectory

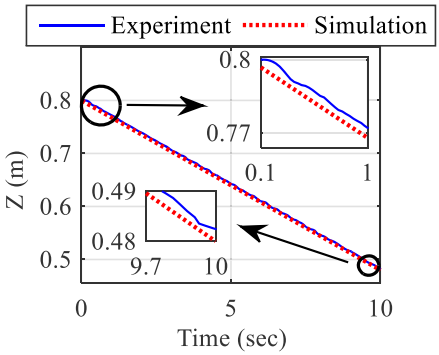

Fig. 30 The end-effector trajectory in Z direction

is 1 cm whereas the simulation figure shows that the position error reaches 4 mm but decreases afterwards. The angular tracking error is demonstrated in Fig. 32, by the norm of Euler angle errors. It is shown that, throughout the operation, the maximum angular error does not exceed 3.5deg.

Control loop delay and limitation in applying the PWM are the two main sources of the error in the system. The delay time is about 30 ms, which is due to the communication delay of serial protocol between the computer and microcontrollers. On the other hand, the internal friction between the gears of the motors limits the minimum required PWM signal. The control signal below the minimum PWM cannot rotate the motor. Specifically, the conventional DC motors used in this study could not reach a speed between a certain minimum value and zero. This status causes an uncertainty for the system model. In addition to the Columb friction between gears, a part of the internal friction also depends on the motor speed. In order to protect the motors, the upper bound of the PWM is restricted. The limitation bound of the 6 motors in the test is as follows

$$\mathbf{PWM}_{\min} = \left[\, 25_{1\times 6} \;\; 10_{1\times 2} \,\right]^T \quad (58)$$

$$\mathbf{PWM}_{\max} = 80_{8\times 1} \quad (59)$$

For further verification of the approach using a measurement system different from the device used for the feedback, another experiment with the following trajectory is performed

$$\mathbf{x} = \left[\, 0 \;\; 0 \;\; 0.75 \;\; \tfrac{20\pi}{180}\sin(\tfrac{2\pi}{10}t) \;\; \tfrac{20\pi}{180}\left(\cos(\tfrac{2\pi}{10}t) - 1\right) \;\; 0 \,\right]^T \quad (60)$$

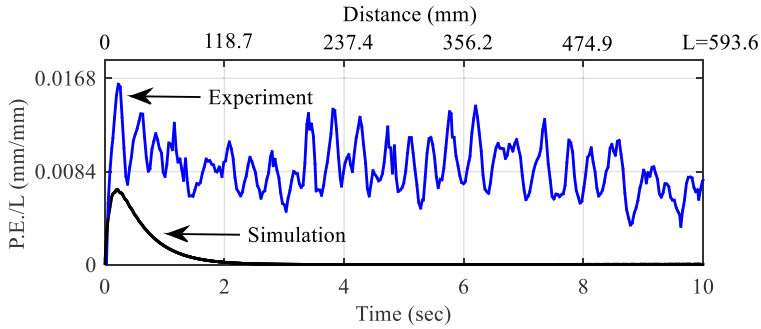

Fig. 31 Position error (P.E.) per total length of trajectory (L)

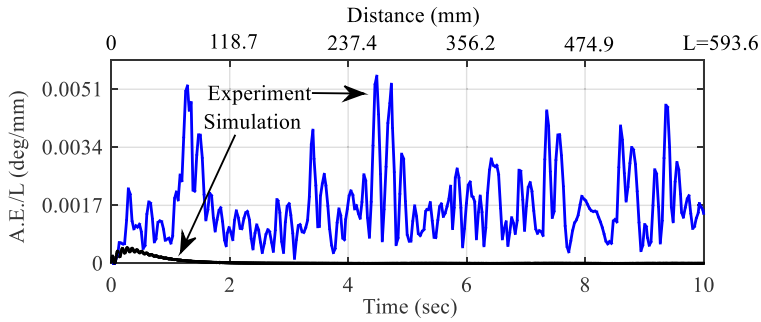

Fig. 32 Norm of Euler angle errors (A.E.) per total length of trajectory (L)

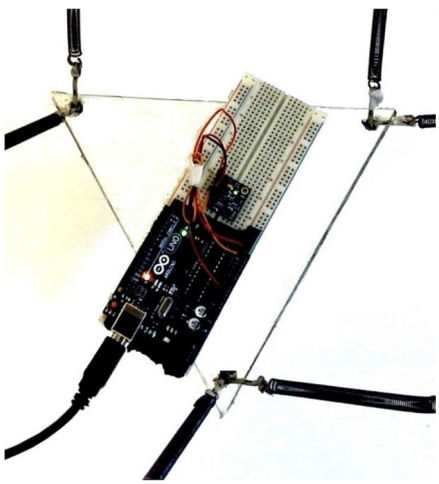

Fig. 33 The IMU mounted on the end-effector

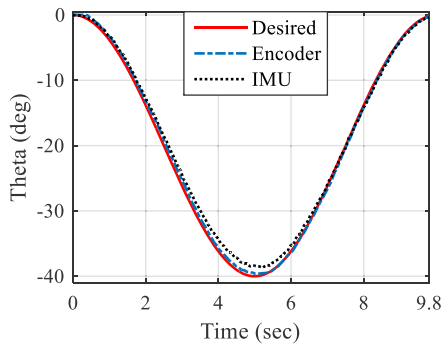

Fig. 35 Pitch angle

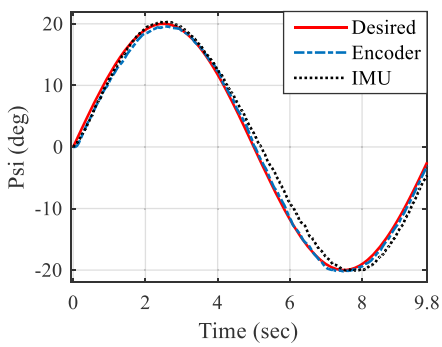

Fig. 34 Roll angle

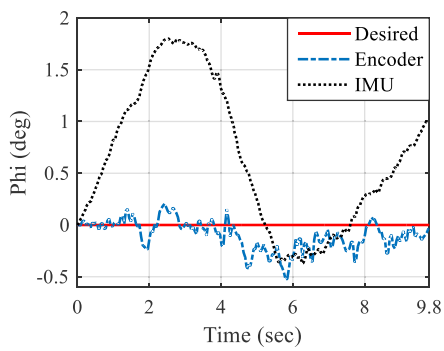

Fig. 36 Yaw angle

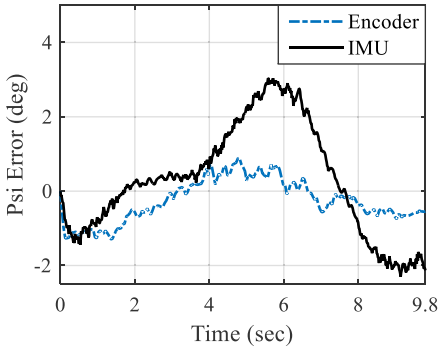

Fig. 37 Roll angle error

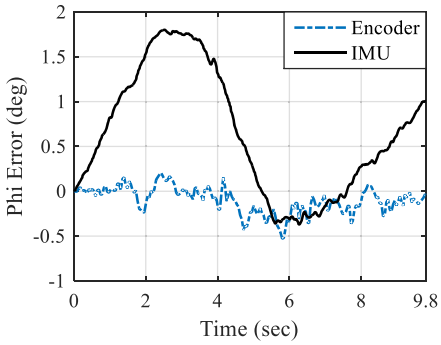

Fig. 39 Yaw angle error

According to Eq. 60, the end-effector position should be maintained constant while its attitude changes periodically. Measurement of the end-effector orientation is performed using an IMU sensor, GY86-MPU 6050, mounted on the end-effector (Fig. 33). Figures 34, 35, and 36 demonstrate that the Euler angles, obtained based on the encoders and IMU, match the desired trajectory with some small errors. According to Figs. 37, 38, and 39, the angular errors estimated using encoders does not exceed 1deg, whereas the errors estimated using IMU sensor reach up to 2deg for the pitch and yaw angles and 3deg for the roll angle. Moreover, it can be observed that the difference between the encoder and IMU measurements is less than 2.5deg. By performing numerous tests, it is observed that the IMU sensor used in this application has repeatability accuracy of nearly 1 deg. Aside from IMU accuracy, the geometrical uncertainties, initial estimate of the end-effector position in workspace and IMU positioning error on the end-effector are the other reasons for the small measurement errors.

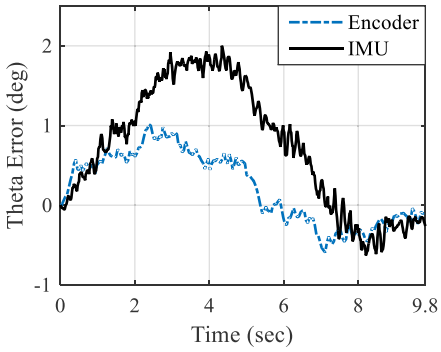

Fig. 38 Pitch angle error

It is known that the end-effector position cannot be estimated using only a low-cost IMU. However, the stationary state of the end-effector position can be demonstrated by mapping the end-effector acceleration from the local frame into the global frame. The percentages of the accelerations per gravity acceleration are shown in Figs. 40, 41, and 42. The noisy state of the accelerations is an intrinsic property of the accelerometers. Nevertheless, the accelerations are very small which shows that the C.G. of the end-effector does not move considerably.

7 Conclusions

In comparison with other types of robots used in load carrying applications, cable robots have larger workspace with lower manufacturing cost. However, larger workspace characteristic may result in more flexibility, due to the increase in the cables length. This issue can lead to the system vibration and degrade the positioning accuracy. Due to the cable flexibility, the number of state variables of the CDPR increases. Therefore, to control the system based on the flexible model, additional feedback such as cable tension or the direct measurement of the end-effector pose as well as the actuator feedback are required. In comparison with rigid controllers, flexible model based controllers requires more sensors and the control input complication enhances the processor computations. On the other hand, in the case of rigid model based controller, the system flexibility adds internal dynamic to the closed loop system. Therefore, it should be shown that the created internal dynamic is stable and also it would not lead to instability of the system

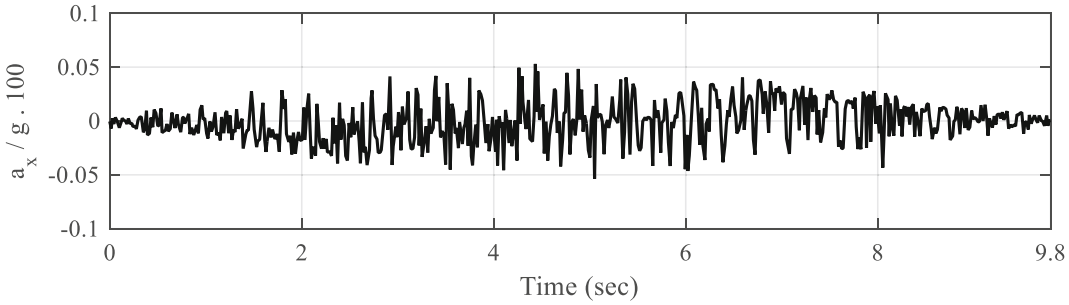

Fig. 40 Translational acceleration a_x

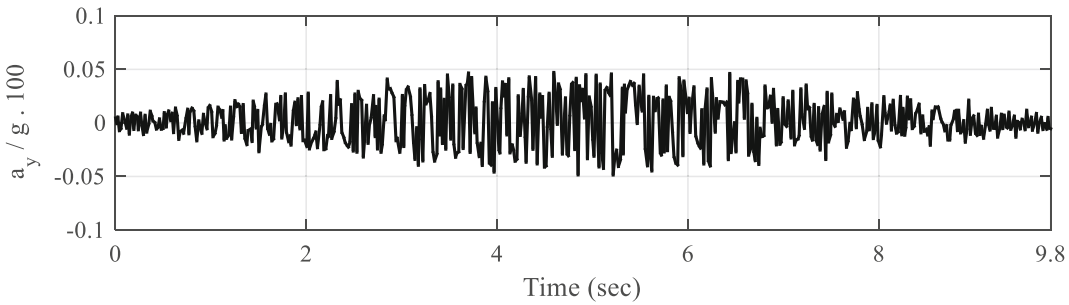

Fig. 41 Translational acceleration a_y

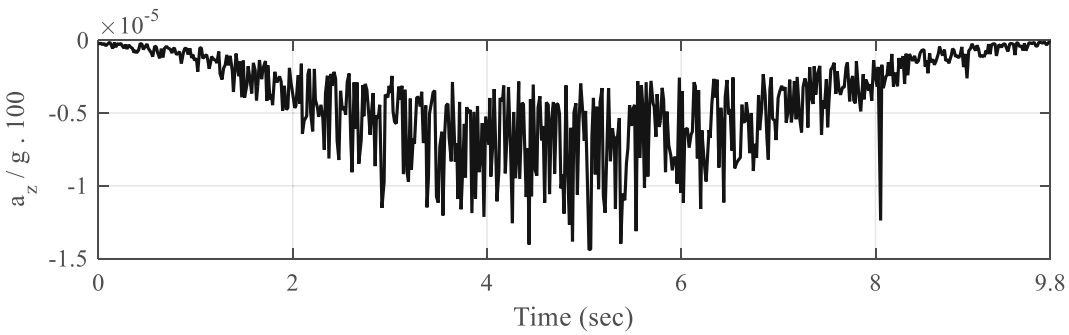

Fig. 42 Translational acceleration a_z

output. To the authors' knowledge, thus far the conditions required for utilizing rigid controllers for flexible CDPRs has not been studied. Therefore, the contribution of this paper compared with the previous studies, is proposing the condition under which the system is stable by solely a rigid model based controller even in the presence of measurement noise. For any controller even robust types, it should be investigated if this condition holds or another condition which guarantees the stability should be found. In addition, the effect of noise uncertainty should be considered in deriving the control laws. In Section 5.2, it is shown that the robust SMC in [7] leads to the system instability in the presence of measurement noise, while the FL+LQG method effectively controls the flexible system. However, to improve the performance of the slow dynamic response of the system the authors are going to develop the controller to an adaptive robust type, as a future work.

In this study, first, the dynamic equations of a cable-suspended robot with viscoelastic cables are obtained. Next, it is shown that using FL controller, obtained based on the rigid model, and fulfillment of a minimum damping coefficient, the system stability is guaranteed. The optimal gains of the controller are obtained using LQR method. The vibration can be considered as a process noise. In addition, measurement noise in the feedback signal is another source of reducing the tracking accuracy. Therefore, in order to compensate for the measurement and process noise, the FL controller is combined with LQG approach. In the simulation section, it is shown that measurement noise or violation of Eq. 34 destabilizes the system controlled by SMC [7] and LQR methods, while LQG method controls the system effectively. Moreover, another simulation demonstrates that the system with damping less than the specified minimum value can be stabilized with the LQG approach, in contrary to the LQR controller.

Verification of the approach is performed by implementation on a laboratory robot manufactured in Iran University of Science and Technology, i.e. ICastBot. In the first test, it is shown that the simulation and experimental results are well matched. The position and angular errors of the experiment are remained below 10 mm and 3.5deg, respectively. The reasons for small errors of the test are identified as the communication delay and restriction in applying the control signal. For further verification, in the second test an attitude control task is performed, where the system output, measured via encoders and IMU sensor, are compared. It is demonstrated that the difference between the Euler angles obtained by the two measurement systems is less than 2.5deg.

Acknowledgments The authors gratefully acknowledge the support of INSF under the grant contracts 93-S-39125.

Appendix

Using Eqs. 11 and 12, the acceleration vector $\ddot{\mathbf{x}}$ can be expressed considering the Euler angles as

$$\ddot{\mathbf{x}} = \mathbf{A_3}\ddot{\mathbf{x}} + \mathbf{A_4} \tag{61}$$

where

$$\mathbf{A_3} = \begin{bmatrix} \mathbf{I_3} & \mathbf{0_3} \\ \mathbf{0_3} & \mathbf{P} \end{bmatrix}, \mathbf{A_4} = \begin{bmatrix} \mathbf{0_{3\times 1}} \\ \dot{\mathbf{P}}\dot{\boldsymbol{\psi}} \end{bmatrix} \tag{62}$$

Considering the Jacobian matrix $\mathbf{\Lambda}$ as

$$\mathbf{\Lambda} = \begin{bmatrix} \cdots & -{}^{\mathbf{N}}\hat{\mathbf{q}}_{\mathbf{i}} & \cdots \\ \cdots & -({}^{\mathbf{N}}\mathbf{R}_{\mathbf{B}}\mathbf{r}_{\mathbf{Bi}}\times{}^{\mathbf{N}}\hat{\mathbf{q}}_{\mathbf{i}}) & \cdots \end{bmatrix}_{6\times 6} \tag{63}$$

the matrices $\mathbf{A_1}$ and $\mathbf{A_2}$ are obtained from

$$\mathbf{A_1} = \frac{1}{r_p}\mathbf{\Lambda}^{TN}\bar{\mathbf{R}}_{\mathbf{B}} \quad where: {}^{\mathbf{N}}\bar{\mathbf{R}}_{\mathbf{B}} = \begin{bmatrix} \mathbf{I_3} & \mathbf{0_3} \\ \mathbf{0_3} & {}^{\mathbf{N}}\mathbf{R}_{\mathbf{B}} \end{bmatrix} \tag{64}$$

$$\mathbf{A_2} = \frac{1}{r_p}\dot{\mathbf{\Lambda}}^{\mathbf{TN}}\bar{\mathbf{R}}_{\mathbf{B}}\dot{\bar{\mathbf{x}}} \tag{65}$$

where ${}^{\mathbf{N}}\hat{\mathbf{q}}_{\mathbf{i}}$ is the unit vector along the i^{th} cable, from motor side to the end-effector side, expressed in the inertial frame. ${}^{\mathbf{N}}\mathbf{R}_{\mathbf{B}}$ is the rotation matrix of the frame attached to the end-effector with respect to the inertial frame.

References

1. Diao, X., Ma, O.: Vibration analysis of cable-driven parallel manipulators. Multibody Sys. Dyn. **21**(4), 347–360 (2009)
2. Zhang, Y., Agrawal, S.K., Piovoso, M.J.: Coupled dynamics of flexible cables and rigid end-effector for a cable suspended robot, American Control Conference (2006)
3. Miermeister, P., Kraus, W., Lan, T., Pott, A.: An elastic cable model for cable-driven parallel robots including hysteresis effects. Mechanisms and Machine Sciences, Cable-Driven Parallel Robots **32**, 17–28 (2015)
4. Arsenault, M.: Workspace and stiffness analysis of a three-degree-of-freedom spatial cable-suspended parallel mechanism while considering cable mass. Mech. Mach. Theory **66**, 1–13 (2013)
5. Huang, P., Zhang, F., Meng, Z., Liu, Z.: Adaptive control for space debris removal with uncertain kinematics, dynamics and states. Acta Astronaut. **128**, 416–430 (2016)
6. Korayem, M.H., Tourajizadeh, H., Bamdad, M.: Dynamic load carrying capacity of cable suspended robot: robust feedback Linearization control approach. J. Intell. Robot. Syst. **60**(3), 341–363 (2010)
7. Korayem, M.H., Taherifar, M., Tourajizadeh, H.: Compensating the flexibility uncertainties of a cable suspended robot using SMC approach. Robotica **33**(3), 578–598 (2015)
8. Laroche, E., Chellal, R., Cuvillon, L., Gangloff, J.: A preliminary study for h_∞ control of parallel cable-driven manipulators, Cable-Driven Parallel Robots, Mechanisms and Machine Science, 353–369 (2013)
9. Meunier, G., Boulet, B., Nahon, M.: Control of an overactuated cable-driven parallel mechanism for a radio telescope application. IEEE Trans. Control Syst. Technol. **17**(5), 1043–1054 (2009)
10. Caverly, R.J., Forbes, J.R.: Dynamic modeling and noncollocated control of a flexible planar cable-driven manipulator. IEEE Trans. Robot. **30**(6), 1386–1397 (2014)
11. Khosravi, M., Taghirad, H.: Dynamic modeling and control of parallel robots with elastic cables: singular perturbation approach. IEEE Trans. Robot. **30**(3), 694–704 (2014)
12. Kosari, S.N., Ramadurai, S., Chizeck, H.J., Hannaford, B.: Control and tension estimation of a cable driven mechanism under different tensions. In: International Design Engineering Technical Conferences and Computers and Information in Engineering Conference, ASME, pp. V06AT07A077–V06AT07A077 (2013)
13. Ramadurai, S., Kosari, S., King, H., Chizeck, H., Hannaford, B.: Application of unscented Kalman filter to a cable driven surgical robot: a simulation study. In: 3rd IEEE International Conference on Robotics and Automation, pp. 1495–1500 (2012)
14. Schenk, C., Bulthoff, H.H., Masone, C.: Robust adaptive sliding mode control of a redundant cable driven parallel robot. In: 19th IEEE International Conference on System Theory, Control and Computing, pp. 427–434 (2015)
15. Tornero, J., Pizh, R., Albertos, P., Salt, J.: Multirate LQG controller applied to self-location and path-tracking in mobile robots. In: Proceedings of the IEEE International Conference on Intelligent Robots and System, vol. 2, pp. 625–630 (2001)
16. Lambert, C., Naho, M.: An aerostat positioning system with cable control. In: 17th World Congress the International Federation of Automatic Control, pp. 779–784 (2008)
17. Berg, J.V.D., Abbeel, P., Goldberg, K.: LQG-MP: optimized path planning for robots with motion uncertainty and imperfect state information. Int. J. Robot. Res. **30**(7), 895–913 (2011)
18. Pota, H., Agrawal, S., Zhang, Y., Petersen, I.: Robust control of residual motion of cable transporter systems, pp. 1446–1451 (2004)
19. Franklin, G.F., Powell, J.D., Emami-Naeini, A.: Feedback Control of Dynamic Systems, 4th edn. Prentice Hall, Englewood Cliffs, NJ (2002)
20. Wang, T., Wang, Q., Hou, Y., Dong, C.: Suboptimal controller design for flexible launch vehicle based on Genetic algorithm: Selection of the weighting matrices Q and R. In: IEEE International Conference on Intelligent Computing and Intelligent Systems, ICIS, vol. 2, pp. 720–724 (2009)
21. Eshtehardiha, S., Kiyoumarsi, A., Ataei, M.: Optimizing LQR and pole placement to control buck converter by Genetic algorithm. In: IEEE International Conference on Control, Automation and Systems, ICCAS'07, pp. 2195–2200 (2007)
22. Verhoeven, R.: Analysis of the Workspace of Tendon-Based Stewart Platforms. Ph.D. Dissertation, University Duisburg-Essen, Essen, Germany (2004)
23. Ouyang, B., Shang, W.W.: A new computation method for the force-closure workspace of cable-driven parallel manipulators. Robotica **33**(3), 537–547 (2015)

M. Habibnejad Korayem was born in Tehran Iran on April 21, 1961. He received his B.Sc. (Hon) and M.Sc. in Mechanical Engineering from the Amirkabir University of Technology in 1985 and 1987, respectively. He has obtained his Ph.D degree in mechanical engineering from the University of Wollongong, Australia, in 1994. He is a Professor in mechanical engineering at the Iran University of Science and Technology. He has been involved with teaching and research activities in the robotics areas at the Iran University of Science and Technology for the last 22 years. His research interests include dynamics of elastic mechanical manipulators, trajectory optimization, symbolic modeling, robotic multimedia software, mobile robots, industrial robotics standard, robot vision, soccer robot, and the analysis of mechanical manipulator with maximum load carrying capacity. He has published more than 600 papers in international journal and conference in the robotic area.

M. Yousefzadeh was born in Iran on December 1976. He received his B.Sc. in Mechanical Engineering from Babol Noshirvani University of Technology in 2000 and then obtained his M.Sc. from K.N. Toosi University of Technology in 2003 in the field of automotive system design. He is currently a PhD student at the department of mechanical engineering in Iran University of Science and Technology in the field of dynamics, vibration and control. His research interests include dynamic, control and vibration analysis of robotic and automotive systems.

B. Beyranvand was born in Iran on June 1991. He received his B.Sc. in Automotive Engineering in 2014 and his M.Sc. in Mechanical Engineering in 2017 from Iran University of Science and Technology. His research interests include vibration and control of robotic systems.